Positive Feedback Between Contractile Ring Myosin and Ring-Directed Cortical Flow Drives Cytokinesis

Renat N. Khaliullin[1]*, Rebecca A. Green[1], Linda Z. Shi[2], J. Sebastian Gomez-Cavazos[1], Michael W. Berns[2], Arshad Desai[1], and Karen Oegema[1]*

[1]Department of Cellular and Molecular Medicine, Ludwig Institute for Cancer Research, University of California, San Diego, La Jolla, CA 92093, USA.

[2]Department of Bioengineering and Institute of Engineering in Medicine, University of California, San Diego, 9500 Gilman Drive, La Jolla, CA, 92093, USA

*Correspondence to: Karen Oegema (koegema@ucsd.edu); Renat N. Khaliullin (renatkh@gmail.com)

ABSTRACT

During cytokinesis, an equatorial actomyosin contractile ring rapidly transforms cell shape by constricting at a relatively constant rate despite its progressively decreasing size. The closure rate per unit length of the ring must accelerate as the ring gets smaller to maintain the overall constant rate of closure. Here, we examine the mechanistic basis for this acceleration by generating a 4D map of cortical flow in conjunction with monitoring ring component dynamics during the first division of the *C. elegans* embryo. This analysis reveals that acceleration arises because ring myosin pulls on the adjacent cortex generating ring-directed cortical flow that, in turn, accelerates constriction by delivering cortical myosin into the ring. We derive an analytical mathematical formulation that captures the positive feedback-dependent evolution of the contractile ring and use this formulation to provide a non-intuitive explanation for why reducing myosin activation by rho kinase inhibition slows contractile ring closure.

IMPACT STATEMENT: During cytokinesis, positive feedback between myosin motors in the contractile ring and ring-directed cortical flow drives constriction rate acceleration to ensure timely cell separation.

MAJOR SUBJECT AREAS: Cell biology, Computational and Systems Biology

KEYWORDS: contractile ring, cortical flow, positive feedback, analytical mathematical model, rho kinase, LET-502, myosin II, anillin

INTRODUCTION

During cytokinesis in animal cells, constriction of an equatorial actomyosin ring cinches the mother cell surface to generate a dumbbell-shaped structure with an intercellular bridge that connects the two daughter cells (Fededa & Gerlich, 2012; Green, Paluch, & Oegema, 2012). The contractile ring assembles in response to the equatorial activation of RhoA (Green et al., 2012; Jordan & Canman, 2012; A. Piekny, Werner, & Glotzer, 2005), which patterns the cortex by recruiting contractile ring components from the cytoplasm (Vale, Spudich, & Griffis, 2009; Yumura, 2001; Zhou & Wang, 2008). Recent work in the *C. elegans* embryo suggests that the equatorial cortex is compressed after this initial patterning, leading to the alignment of actin filament bundles as the ring forms (Reymann, Staniscia, Erzberger, Salbreux, & Grill, 2016). After its assembly, the ring is thought to progressively disassemble as it constricts (Murrell, Oakes, Lenz, & Gardel, 2015; Schroeder, 1990). Ring constriction must complete within a short cell cycle window during mitotic exit (Canman, Hoffman, & Salmon, 2000; Martineau, Andreassen, & Margolis, 1995; Straight et al., 2003). Timely constriction relies on the conserved ability of contractile rings to maintain a relatively constant closure rate despite their progressively decreasing perimeter (Biron, Libros, Sagi, Mirelman, & Moses, 2004; Bourdages, Lacroix, Dorn, Descovich, & Maddox, 2014; Calvert et al., 2011; Carvalho, Desai, & Oegema, 2009; Ma et al., 2012; Mabuchi, 1994; Pelham & Chang, 2002; Zumdieck, Kruse, Bringmann, Hyman, & Julicher, 2007). This property implies that rings close at a faster rate per unit length as they get smaller. Prior work postulated that this acceleration arises because force generators, either myosin motors (Wu & Pollard, 2005) or actin filament-based contractile units (Carvalho et al., 2009), are retained during constriction, leading to an increase in their amount per unit length. This retention model presumes that acceleration arises from processes intrinsic to the contractile ring, ignoring potential influence of interactions between the ring and the adjacent cortex.

Here, we examine the role of interactions between the ring and surrounding cortex on contractile ring dynamics in the *C. elegans* embryo. Through 4D analysis of cortical flow in conjunction with monitoring of ring component dynamics during closure, we show that acceleration of the per unit length constriction rate does not arise from ring-intrinsic component retention, but instead results from positive

feedback between ring myosin and ring-directed cortical flow. We derive an analytical mathematical formulation that captures the positive feedback-dependent evolution of the contractile ring and employ it to analyze experimental data to assess the effects of rho kinase inhibition, uncovering a new, non-intuitive explanation for why reducing myosin activation by rho kinase inhibition slows ring closure.

RESULTS

The cortex at the cell poles expands in response to tension generated by the constricting ring, whereas the intervening cortex flows towards the ring without expansion

To assess the significance of interactions between the contractile ring and surrounding cortex on contractile ring dynamics, we generated a 4D map of cortical flow to determine how the cortex responds to ring pulling. We monitored cortical movement at high time resolution (**Figure 1A, Video 1**) in embryos expressing a GFP fusion with the heavy chain of non-muscle myosin II (NMY-2; hereafter myosin::GFP; Figure 1 – Figure **Supplements 1, 2**), while also monitoring ring constriction at lower time resolution in the same embryos (**Figure 1A, Figure 1 – Figure Supplement 3**). Myosin::GFP flowed together with actin (LifeAct::mKate2) on the embryo surface (**Figure 1 – Figure Supplement 4)**, consistent with prior work indicating that the entire cell surface, from cortex-associated cytoplasmic granules to cell surface receptors, moves in a coordinated fashion during cytokinesis (Cao & Wang, 1990; DeBiasio, LaRocca, Post, & Taylor, 1996; Fishkind, Silverman, & Wang, 1996; Hird & White, 1993; Reymann et al., 2016; Swann & Mitchison, 1958; Wang, Silverman, & Cao, 1994). Because the contractile ring closes asymmetrically within the division plane ((Maddox, Lewellyn, Desai, & Oegema, 2007); **Figure 1A, Figure 1 – Figure Supplement 3**), the pattern of cortical movement cannot be inferred from imaging individual embryos. Therefore, we generated an average 4D map of cortical flow by computationally combining data from 93 embryos imaged in random rotational orientations (**Figure 1A, Figure 1 – Figure Supplement 3**). We defined the top of the embryo as the side where the furrow ingresses first, the bottom as the opposite side, and referenced positions around the embryo circumference by the angle θ. For temporal alignment, we fit a line to normalized ring size ($\bar{R} := R/R_{emb}$) versus time between 30% and 80% closure for each embryo, and extrapolated this line to 1 and 0 to define t_0 (cytokinesis onset) and t_{CK} (time of cytokinesis), respectively (**Figure 1A, Figure 1 – Figure Supplement 3**). Cortical flow could not be monitored in the division plane or at the cell poles, due to their high curvature. Thus, this approach provided a quantitative picture of cortical movement in the central 2/3 of the embryo throughout cytokinesis (**Figure 1B**; **Video 2**).

93 The 4D map of cortical flow allowed us to determine where new cortical surface is gained as the
94 ring closes. New cortical surface could be gained uniformly, immediately behind the contractile ring, or at
95 the cell poles (Bluemink & de Laat, 1973; Byers & Armstrong, 1986; Danilchik, Bedrick, Brown, & Ray,
96 2003; Gudejko, Alford, & Burgess, 2012; Selman & Perry, 1970; Swann & Mitchison, 1958; Turlier,
97 Audoly, Prost, & Joanny, 2014; Zumdieck et al., 2007), with each pattern predicting a different profile of
98 cortical velocity along the embryo axis (**Figure 1 – Figure Supplement 5**). The cortical velocity profiles
99 measured from the flow map indicated that cortical surface is gained at the poles and subsequently
100 moves with constant velocity towards the division plane (**Figure 1B**). The velocity of cortical flow was
101 higher on the top of the embryo during the first half of cytokinesis when the furrow ingresses from the top
102 (**Figure 1B, black traces**) and became higher on the bottom of the embryo towards the end when the
103 furrow ingresses from the bottom (**Figure 1B, grey traces; Video 2**).
104 Cutting the cortex parallel or perpendicular to the division plane using a laser revealed that the
105 cortex is under tension during cytokinesis (**Figure 2A**). However, parallel laser cuts had no effect on the
106 constriction rate (**Figure 2B,C**) indicating that cortical tension does not impose significant resistance to
107 ring pulling. Inhibiting the Arp2/3 complex by depleting its ARX-2 subunit, which is expected to reduce
108 effective cortical viscosity and thus cortical tension (Chaudhuri, Parekh, & Fletcher, 2007; Davies et al.,
109 2014; Tseng & Wirtz, 2004), also did not alter the constriction rate (**Figure 2 – Figure Supplement 1**).
110 Together, these results indicate that the cortex at the poles expands in response to tension generated by
111 the constricting ring, whereas the cortex in the region between the ring and the poles flows towards the
112 ring without expansion or compression. This differential response of the polar cortex to ring-generated
113 tension, which results in a flow of myosin and other cortical components towards the cell equator, is
114 consistent with the idea of polar relaxation hypothesized in early conceptual models of cytokinesis
115 (Greenspan, 1978; Swann & Mitchison, 1958; Taber, 1995; White & Borisy, 1983; Wolpert, 1960;
116 Zinemanas & Nir, 1987, 1988).
117
118 ***The contractile ring pulls in extra cortex during constriction, leading to an exponential increase in***
119 ***the levels of ring components and in the ring constriction rate***

120 Recent work in the *C. elegans* embryo suggested that recruitment of contractile ring proteins
121 following anaphase onset leads to compression of the equatorial cortex that aligns actin filaments to form
122 the contractile ring (Reymann et al., 2016). Consistent with this, a gradient of cortical flow velocity that
123 spans the cell equator is observed in our flow map at early timepoints prior to furrow ingression (**Figure 2**
124 **– Figure Supplement 2**). After contractile ring assembly, the ring has been proposed to constrict in an
125 autonomous manner via continuous disassembly (Murrell et al., 2015; Schroeder, 1975). In this view, the
126 constricting ring would generate the division plane by pulling the cortex behind it, and the amount of
127 cortex entering the division plane would equal the area of the division plane. To test this prediction, we
128 analyzed the 4D cortical flow map to measure the total cortical surface area entering the division plane
129 and compare it to the area of the division plane (accounting for the fact that two surfaces are generated-
130 *red outline in* **Figure 3A**). Surprisingly, this analysis revealed that significantly more cortical surface
131 entered the division plane than is necessary to build the plane: the flux of cortical area into the division
132 plane was 1.5 to 2-fold higher than the rate of change in the area of the division plane throughout
133 cytokinesis (**Figure 3A,B**). In control embryos, more cortex flowed in from the posterior side than from
134 the anterior side, likely due to distinct mechanical cortical properties downstream of the polarity
135 machinery. Consistent with this, and with prior work showing that Arp2/3 inhibition impairs the
136 recruitment of PAR-2 to the posterior cortex and makes myosin and actin dynamics on the posterior
137 cortex more similar to those in embryo anterior (Xiong, Mohler, & Soto, 2011), inhibiting the Arp2/3
138 complex by depleting ARX-2 abolished the difference between the two sides, but did not change the
139 imbalance between the total amount of cortex entering the division plane and the area of the plane
140 (**Figure 3 – Figure Supplement 1; Video 3**). Thus, significantly more cortical surface enters the division
141 plane during cytokinesis than expected if the cortex passively trails behind the closing ring (**Figure 3A**).
142 The extra cortex delivered into the division plane could concentrate in the ring and contribute to
143 its closure, distribute within the division plane, or be lost due to disassembly (**Figure 3C**). To distinguish
144 between these and other possibilities, we monitored *in situ*-tagged myosin::GFP (Dickinson, Ward,
145 Reiner, & Goldstein, 2013) (**Figure 3D**) and GFP::anillin (**Figure 3 – Figure Supplement 2**) in the
146 division plane. Both probes exhibited similar behavior, accumulating primarily within the ring (**Figure 3D,**

147 **Figure 3 – Figure Supplement 3**). Quantification of mean per unit length fluorescence around the ring
148 (after attenuation correction; **Figure 3 – Figure Supplement 4**) revealed a steady increase for both
149 markers as constriction proceeded. The increase began on the top, which ingresses first, and initiated
150 later on the bottom, which ingresses after the constriction midpoint (**Figure 3D, Figure 3 – Figure**
151 **Supplement 3**). Thus, monitoring of myosin and anillin suggests that the extra cortical surface flowing
152 into the division plane is incorporated into the ring and predicts that the amount of ring myosin and anillin
153 should increase in proportion to the flux of extra cortical surface into the ring (**Figure 3E**). To test this
154 prediction, we compared the per unit length rate of ring-directed cortical flow to the per unit length
155 amounts of myosin and anillin. All were well-fit by the same single exponential (**Figure 3E,F**), consistent
156 with the idea that cortical surface flowing into the division plane delivers components to the contractile
157 ring during constriction.

158 The exponential increase in the per unit length levels of ring myosin and anillin during constriction
159 (**Figure 3F**) is best explained by positive feedback: ring myosin pulls in adjacent cortex, bringing
160 additional myosin motors into the ring that in turn increase the velocity of ring-directed cortical flow
161 (**Figure 3G**). The per unit length constriction rate also increases with the same exponential kinetics as
162 the per unit length rate of ring-directed cortical flow and the per unit length amounts of anillin and myosin
163 (**Figure 3H**). This coupling likely arises because the constriction rate, like the rate of ring-directed cortical
164 flow, depends on the amount of ring myosin. The exponential increase in the per unit length constriction
165 rate explains the ability of contractile rings to close at a relatively constant rate despite their progressively
166 decreasing perimeter (Biron et al., 2004; Bourdages et al., 2014; Calvert et al., 2011; Carvalho et al.,
167 2009; Ma et al., 2012; Mabuchi, 1994; Pelham & Chang, 2002; Zumdieck et al., 2007). A relatively
168 constant rate of closure is observed over a significant portion of ring constriction (**Figure 1A**; $t = 50$-
169 200s) because the exponential increase in the per unit length constriction rate balances the decrease in
170 ring size.

171

172 ***Component levels and fluorescence recovery after photobleaching of the division plane support***
173 ***constriction rate acceleration due to ring-directed flow versus component retention***

174 Our results indicate that the per unit length amount of contractile ring components increases
175 exponentially, and suggest that this increase is due to delivery by cortical flow along the direction
176 perpendicular to the ring. In this model, constriction in the around-the-ring direction does not alter the per
177 unit length amount of ring components, but instead drives ring disassembly that reduces the total amount
178 of ring components in proportion to the reduction in ring length (**Figure 4A, left panel**). An alternative
179 model for the increase in the per unit length amount of ring components, proposed based on work in
180 fission yeast (Wu & Pollard, 2005), is that myosin and anillin could be retained within the ring rather than
181 lost as ring perimeter decreases during constriction (**Figure 4A, middle panel**). In the retention model,
182 the total amounts of both components remain constant as the ring closes resulting in an increase in their
183 per unit length amount that is inversely proportional to the reduction in ring size. Comparison with the
184 total amounts of ring myosin and anillin suggested that, whereas the retention model fits the data well for
185 t/t_{ck} between 0.2 and 0.6, there was significant deviation for timepoints outside of this range. In contrast,
186 the ring-directed cortical flow model fit the data for the entire measured interval (t/t_{ck}= 0.0 to 0.8; **Figure**
187 **4B, Figure 3 – Figure Supplement 3**).

188 To distinguish between the retention and ring-directed flow models using an independent
189 approach, we photobleached myosin in the entire division plane at ~30% closure, and monitored its
190 subsequent recovery in the ring (**Figure 4C**). The ring-directed cortical flow model predicts that the per
191 unit length amount of bleached myosin should be constant and, since cortical myosin turns over faster
192 than myosin in the ring ($t_{1/2}$ of ~30s (Mayer, Depken, Bois, Julicher, & Grill, 2010; Salbreux, Charras, &
193 Paluch, 2012)), cortical flow should rapidly deliver unbleached fluorescent myosin to the ring, leading to
194 an exponential increase comparable to that in controls. In contrast, the retention model predicts that the
195 per unit length amount of bleached myosin and any residual fluorescent myosin that is retained in the
196 ring will increase in proportion to the decrease in the ring size (~1/R). We found that the per unit length
197 amount of fluorescent myosin in the ring increased exponentially following bleaching, and the difference
198 between the control and the bleached embryos, which reflects the amount of bleached myosin, remained
199 constant, both of which agree with the predictions of the ring-directed cortical flow model (**Figure 4C**).
200 We note that this data also suggests that the recovery of myosin fluorescence in the ring in not due to

201 exchange with myosin in the cytoplasm. If ring myosin were turning over due to exchange with
202 cytoplasmic myosin, we would expect the FRAP curve to approach the control curve and the difference
203 between the FRAP and control curves to disappear. Instead, the two curves remained parallel and the
204 difference remained constant (**Figure 4C**). This data suggest that rather than being due to exchange with
205 cytoplasmic myosin, the recovery of ring fluorescence is due to a mechanism in which myosin on the
206 cortex adjacent to the ring turns over, allowing resumption of delivery of myosin to the ring by cortical
207 flow.

208 The conclusion that the per unit length amount of contractile ring components increases
209 exponentially during constriction is in apparent contradiction to analysis in 4-cell stage *C. elegans*
210 embryos, where we had previously reported an ~1.3-fold increase in myosin, anillin and septins as the
211 ring perimeter decreased 2-fold (from 50 to 25 μm). However, this is in fact consistent with the prediction
212 of the ring-directed cortical flow model (see **Figure 4 – Figure Supplements 1, 2** for an analysis of ring
213 component levels and recovery following photobleaching at the 4-cell stage).

214 Together these data suggest that, the acceleration of the per unit length constriction rate during
215 closure, a conserved feature of contractile rings, does not arise from ring component retention, but from
216 positive feedback between ring myosin and ring-directed cortical flow.

217

218 ***An analytical mathematical formulation for the positive feedback-mediated evolution of the***
219 ***contractile ring***

220 The exponential accumulation of contractile ring components during constriction due to positive
221 feedback means that the properties of the ring (component levels and constriction rate) are continuously
222 changing. Thus, analysis of perturbations requires fitting temporal profiles of ring size or component
223 levels and deriving meaningful quantitative parameters from these fits. In order to assess the
224 consequences of molecular perturbations, we therefore translated our experimental findings
225 (summarized in **Figure 5A**) into an analytical mathematical framework (see **Methods** for detailed
226 derivation), consisting of three equations and three model parameters, that we named the Cortical Flow
227 Feedback (CoFFee) model (**Figure 5B**). Based on our photobleaching data, we assume that: (1)

228 constriction in the around-the-ring direction does not alter the per unit length amount of ring components,
229 but leads to ring disassembly that reduces the total amount of ring components in proportion to the
230 reduction in ring length, and (2) myosin in the contractile ring does not turn over by exchange with
231 myosin in the cytoplasm. Thus, increases in the per unit length amount of ring myosin are solely due to
232 delivery by cortical flow along the direction perpendicular to the ring. We posit that myosin increases
233 exponentially during constriction due to positive feedback between the per unit length amount of ring
234 myosin and the velocity of cortical flow that delivers myosin into the ring. Positive feedback arises from
235 the fact that the velocity of ring-directed cortical flow is proportional to the amount of ring myosin, and the
236 amount of ring myosin increases in proportion to the velocity of cortical flow (**Figure 5A**). In our
237 mathematical formulation, the velocity of ring-directed cortical flow ($v_{flow}(t)$) is related to the amount of
238 ring myosin ($M_{ring}(t)$, per unit length) by a proportionality constant α that reflects the ability of the cortex
239 to be compressed (**Figure 5B,** Eqn. (1)), and ring myosin increases at a rate proportional to the velocity
240 of ring-directed cortical flow and the concentration of cortical myosin (m_{cort}; **Figure 5B**, Eqn. (2)). As a
241 result of the positive feedback, ring myosin increases exponentially with a characteristic time $\tau :=$
242 $1/\alpha m_{cort}$ (time required for ring myosin to increase ~2.7 fold; **Figure 5B, lower left**). The per unit length
243 constriction rate is proportional to the amount of ring myosin, being related by a constant β that reflects
244 the ability of the ring to be constricted (**Figure 5B,** Eqn. (3)).

245 To obtain expressions for contractile ring size and component levels that can be used to fit data,
246 we solved the model equations in a specific time reference. Instead of $t = 0$ being defined by
247 extrapolation of plots of $\bar{R}$ $(:= R/R_{emb})$ versus time (**Figure 1A**), which is not ideal in a mathematical
248 formulation, we set $t = 0$ as the halfway point of ring closure ($\bar{R}(t = 0) = \frac{1}{2}$). This time reference also
249 avoids the difficulty of assessing cytokinesis onset. In this time reference, the equation for ring size is:

$$\bar{R}(\bar{t}) = \bar{R}_{ini}(2\bar{R}_{ini})^{-\exp(\bar{t})}, \tag{4}$$

250 where $\bar{t} := t/\tau$ and $\bar{R}_{ini}$ is the dimensionless characteristic ring size (held fixed at a value of 1.1; see
251 Methods). Any component that localizes to the cell cortex will be delivered to the contractile ring via the
252 same process as myosin, so contractile ring components all accumulate in a similar fashion, with

$$C_{ring}(\bar{t}) - C_{ring,base} = \frac{\alpha c_{cort}}{\beta} \ln(2\bar{R}_{ini})\, \mathrm{e}^{\bar{t}}, \tag{5}$$

$$C_{ring,base} := C_{0,ring} - \ln(2\bar{R}_{ini}) \frac{\alpha c_{cort}}{\beta}, \tag{6}$$

253 where $C_{0,ring}$ is the per unit length amount of the component at the half-way point of ring closure,
254 $C_{ring,base}$ is the baseline amount of the ring component that does not increase exponentially, and c_{cort}
255 (m_{cort} for myosin) is the concentration of the component on the cortex that is delivered to the ring. The
256 velocity of cortical flow and the constriction rate are

$$v_{flow}(\bar{t}) = \frac{\alpha}{\beta} \ln(2\bar{R}_{ini})\, \mathrm{e}^{\bar{t}}, \tag{7}$$

$$-\frac{1}{\bar{R}} \frac{d\bar{R}}{d\bar{t}} = \ln(2\bar{R}_{ini})\, \mathrm{e}^{\bar{t}}. \tag{8}$$

257 Thus, the per unit length constriction rate, velocity of cortical flow, and ring component amounts
258 all increase exponentially with the characteristic time of ring myosin accumulation ($\tau = 1/\alpha m_{cort}$) set by
259 the feedback loop between ring myosin and cortical flow (**Figure 5B**), as we observe experimentally
260 (**Figure 3E-H**).
261

262 ***Reducing the concentration of cortical myosin reduces the ability of the ring to be constricted by***
263 ***ring myosin***

264 To address the effect of reducing myosin activation on cytokinesis, we used our mathematical
265 formulation to analyze the effects of depleting rho kinase (LET-502). Rho kinase contributes to myosin
266 activation by promoting regulatory light chain phosphorylation. Due to parallel pathways for myosin
267 activation, penetrant rho kinase inhibition slows, but does not prevent, ring constriction (Maddox et al.,
268 2007; Matsumura, 2005; A. J. Piekny & Mains, 2002). We imaged control and rho kinase-depleted
269 embryos expressing *in situ* tagged myosin::GFP. To assess the impact of rho kinase inhibition on the
270 properties of the ring and cortex encoded in our three model parameters (α, β, and m_{cort}), we directly
271 measured m_{cort} and fit experimental measurements of ring size and ring myosin versus time to
272 equations (4) and (5) to determine the effects on α and β (**Figure 6A**). Direct measurement revealed that

273 the amount of cortical myosin, m_{cort}, was reduced by 20% in rho kinase depleted embryos compared to
274 controls ($m_{cort}^{RKdep} = 0.8\, m_{cort}^{WT}$; **Figure 6B**). Next, we fit traces of ring size versus time using the ring size
275 equation (4) to determine characteristic times, ($\tau = 1/\alpha m_{cort}$), for each embryo. This analysis revealed
276 that τ was 1.3-fold higher in rho kinase-depleted embryos compared to controls (120 ± 20 s versus
277 90 ± 10 s in controls; **Figure 6C, middle row**) indicating that $\alpha^{RKdep}\, m_{cort}^{RKdep} = 0.8\, \alpha^{WT}\, m_{cort}^{WT}$. Since
278 $m_{cort}^{RKdep} = 0.8\, m_{cort}^{WT}$, we conclude that $\alpha^{RKdep} = \alpha^{WT}$; thus, the ability of the cortex to be compressed by
279 ring myosin is not affected by rho kinase depletion. To determine the effect on β, we measured the mean
280 per unit length amount of myosin::GFP in the ring versus time in control and rho kinase depleted
281 embryos and fit the data to the equation for ring myosin (5). Interestingly, the per unit length amount of
282 myosin for a given ring size was the same in control and rho kinase depleted embryos, resulting in an
283 equivalent exponential prefactor for the two conditions ($\alpha^{RKdep}\, m_{cort}^{RKdep}/\beta^{RKdep} = \alpha^{WT}\, m_{cort}^{WTp}/\beta^{WT}$;
284 **Figure 6C, bottom row, Figure 6 – Figure Supplement 1**). From this we conclude that the ability of the
285 ring to be constricted by ring myosin is reduced in rho kinase depleted embryos compared to controls
286 ($\beta^{RKdep} = 0.8\, \beta^{WT}$).

287 The effects of rho kinase inhibition identified by our analysis are schematically summarized in
288 Figures 7A and B. Rho kinase inhibition decreases the concentration of cortical myosin, m_{cort} , to 80% of
289 its value in controls, which slows myosin accumulation via the feedback loop and increases τ.
290 Normalizing time by τ and setting $\bar{t} = 0$ at 50% closure superimposes the constriction rate curve with the
291 control (**Figure 7B, Figure 7 – Figure Supplement 1**). This is a convenient reference frame for
292 comparing two conditions because comparing component levels and flow velocity at the same $\bar{t}$
293 corresponds to comparing them for the same ring size. Perturbations that reduce the ability of the ring to
294 be constricted by ring myosin (reduce β) introduce a time delay between cortical flow/accumulation of
295 contractile ring components and the constriction rate (see **Figure 7 – Figure Supplement 2** for detailed
296 explanation). The length of the delay is the amount of time it takes for the feedback loop to accumulate
297 enough ring myosin to compensate for the reduction in β. After the delay, ring closure proceeds with
298 kinetics identical to controls but with higher flow velocities and ring component concentrations. Due to the
299 reduction in β in rho kinase depleted embryos, the velocity of cortical flow is predicted to be 1.25 fold

300 higher for all ring sizes in the $\bar{t}$ reference frame (**Figure 7B**, middle panel). Thus, our analysis suggests
301 that the per unit length amount of myosin is the same for rings of all sizes in control and rho kinase
302 depleted embryos (**Figure 6C**) because there is an increase in the amount of cortical flow into the ring
303 that compensates for the reduction in the concentration of cortical myosin (**Figure 7B**, last panel).

304 Filming control and rho kinase depleted embryos expressing GFP::anillin and measuring the
305 concentration of cortical anillin ($c_{ani,cort}$) revealed that it is not altered by rho kinase inhibition. Thus, if
306 our prediction that there is more cortical flow into the ring in rho kinase depleted embryos is correct, the
307 per unit length amount of cortical anillin should be 1.25-fold higher in rings of all sizes in rho kinase
308 depleted embryos compared to control embryos. Consistent with this prediction, measurement of mean
309 per unit length GFP::anillin fluorescence in the ring revealed a 1.21 fold increase (**Figure 7C, Figure 6 –**
310 **Figure Supplement 1**). Thus, an analysis of rho kinase-depleted embryos employing the mathematical
311 formulation of the positive feedback model for cytokinetic ring closure leads to the counterintuitive
312 conclusion that reducing the concentration of cortical myosin makes it more difficult for rings of the same
313 size with the same amount of myosin to constrict. We suggest that this may be because the
314 compensatory increase in cortical flow that restores ring myosin to control levels leads to an
315 overabundance of other components (e.g. anillin) that increase resistance of the ring to constriction.
316 More broadly, the analysis of rho kinase inhibition, employing straightforward-to-measure experimental
317 parameters, highlights the utility of the mathematical formulation we present to explain the complex and
318 non-intuitive effects of molecular perturbations on cytokinesis.
319

320 **DISCUSSION**

321 Despite the physical connection between the contractile ring and adjacent cortex, how these
322 interconnected regions function together to change cell shape during cytokinesis has not been clear.
323 Here, we explore this question during the first division of the *C. elegans* embryo by generating a 4D map
324 of cortical flow in conjunction with laser ablation experiments and monitoring of ring component dynamics
325 in the division plane. Our results indicate that polar relaxation collaborates with cortical contractility at the
326 cell equator to enable the assembly and subsequent structural evolution during constriction of the
327 contractile ring. In particular, we show that the pattern of polar relaxation and equatorial contractility set
328 up by spindle-based signaling generates a positive feedback loop between ring myosin and ring-directed
329 cortical flow that feeds the ring. The resulting exponential increase in the per unit length constriction rate
330 explains the ability of the ring to close at a relatively constant overall rate despite its progressively
331 decreasing perimeter during constriction. The broad conservation of this property (Biron et al., 2004;
332 Bourdages et al., 2014; Calvert et al., 2011; Carvalho et al., 2009; Ma et al., 2012; Mabuchi, 1994;
333 Pelham & Chang, 2002; Zumdieck et al., 2007), which allows cytokinesis to complete in a temporally
334 restricted cell cycle window (Canman et al., 2000; Martineau et al., 1995; Straight et al., 2003), suggests
335 that feedback between contractile ring myosin and ring-directed cortical flow will be a broadly conserved
336 property of contractile rings in animal cells. The feedback-based mechanism we describe here, in which
337 the increase in myosin levels in the ring is due to cortical flow along the direction perpendicular to the
338 ring contrasts with prior models, including a model previously proposed by our group, that constriction
339 rate acceleration arises from the ring-intrinsic retention of force generating units (Carvalho et al., 2009;
340 Wu & Pollard, 2005).

341 In addition to ensuring timely cell content partitioning, the feedback-based mechanism that we
342 describe renders the ring robust to defects in the cytokinesis machinery that increase the difficulty of ring
343 constriction, such as in the inhibition of rho kinase that we investigate here, and/or to internal or external
344 mechanical challenges, such as cell-cell contacts or obstacles in the crowded cell interior. In all of these
345 cases, the feedback loop between ring myosin and cortical flow would lead to the progressive build up of
346 contractile ring components until constriction proceeded. An interesting caveat, suggested by modeling

347 (**Figure 7—figure supplement 2**) is that molecular perturbations that reduce the ability of the ring to be
348 constricted by ring myosin (reduce β in the mathematical formulation) do not alter the kinetics of
349 contractile ring closure. Instead, they introduce a time delay that allows the ring to accumulate enough
350 myosin to overcome the reduced β. After this delay, constriction proceeds with kinetics identical to
351 controls, but with higher component levels and flow velocities throughout closure. Experimentally, this
352 means that perturbations that make ring constriction more difficult will not be detected by monitoring
353 constriction kinetics in the absence of a reliable time reference for cytokinesis onset, since the introduced
354 delay may be relatively small. The second signature feature of these perturbations, higher component
355 levels throughout closure, would likely be easier to measure (e.g., by quantifying ring component levels
356 at the closure halfpoint).

357 We note that ring-directed flows have also been observed in the context of wound healing
358 (Mandato & Bement, 2003), and similar types of cortical dynamics driven by coordinated patterns of
359 contractility and relaxation are relevant in many contexts including cell polarization, cell motility, and
360 tissue morphogenesis (Gardel, Schneider, Aratyn-Schaus, & Waterman, 2010; Munjal & Lecuit, 2014;
361 Salbreux et al., 2012), suggesting that the positive feedback between myosin in contractile structures
362 and cortical flow will act in physiological contexts beyond cytokinesis.

363

364 ***Polar relaxation enables ring-directed cortical flow that feeds the contractile ring during***
365 ***constriction***

366 The cortical flow map and laser ablation analysis indicate that recruitment of myosin to the
367 equatorial cortex leads to local compression that places the adjacent cortex under tension. In response
368 to this tension, the polar cortex expands; in contrast, the cortex between the poles and the equator flows
369 towards the ring without expanding. These observations suggest that the polar cortex has distinct
370 mechanical properties. These distinct properties could arise from different, non-exclusive mechanisms.
371 The polar cortex may be less stiff than the rest of the cortex, causing it to stretch and thin in response to
372 ring constriction-induced tension. Consistent with this idea, a reduction in f-actin intensity at the cell poles
373 has been reported during cytokinesis in *Drosophila* cells due to delivery of a phosphatase by segregating

374 chromosomes (Rodrigues et al., 2015). Alternatively, the polar cortex may turnover more rapidly, leading
375 to a higher rate of surface renewal after stretching. A third possibility is that the polar cortex is more
376 prone to rupture, repair of which would locally increase cortical surface. Consistent with this last idea,
377 blebs have been reported at the cell poles in cultured vertebrate and *Drosophila* cells, where they have
378 been proposed allow cells to elongate in anaphase and release tension at the poles (Hickson, Echard, &
379 O'Farrell, 2006; Sedzinski et al., 2011). Understanding precisely how the polar cortex is different in
380 molecular and mechanical terms, and the mechanisms that generate these differences are important
381 goals for future work.

382 Early conceptual models of cytokinesis hypothesized that polar relaxation coupled to a global
383 upregulation of surface tension could trigger a flow of tension-generating elements towards the equator
384 that would compress into a circular band and initiate a feedback loop similar to the one we describe here
385 (Greenspan, 1978; Swann & Mitchison, 1958; Taber, 1995; White & Borisy, 1983; Wolpert, 1960;
386 Zinemanas & Nir, 1987, 1988). Although polar relaxation could drive cytokinesis on its own, the
387 compressed band of cortex would be sensitive to the mechanical properties of the cortex and the amount
388 and timing of relaxation at each pole. Any non-uniformity, for example due to cell-cell contacts, could
389 lead to unstable positioning or collapse of the ring to one side (Greenspan, 1978). Similarly, mechanisms
390 that promote cortical contractility at the cell equator could initiate ingression; however, in the absence of
391 cortical relaxation, cytokinesis would stall due to progressively increasing cortical tension. Coupling
392 equatorial contractility to polar relaxation, as we observe in the *C. elegans* embryo, has two beneficial
393 effects: (1) it releases the isotropic tension produced by compression of the equatorial cortex along the
394 direction perpendicular to the ring, leading to filament alignment and ring narrowing that reduces
395 resistance from cytoplasmic pressure and, (2) it allows the ring to establish a pattern of ring-directed
396 cortical flow to generate a feedback loop that provides components to the ring in proportion to the
397 velocity of cortical flow rather than the rate of network turnover.

398 Information on constriction kinetics and patterning of cortical compression/expansion suggests
399 that a similar coupling may also support ring constriction in sea urchin embryos. Cleaving sea urchin
400 embryos from a variety of species exhibit constriction kinetics essentially identical to those during the first

division of the *C. elegans* embryo (Mabuchi, 1994). Pioneering work by Katsuma Dan monitoring surface expansion and compression by measuring the distance between surface-adhered particles and the distribution of pigmented cortex-associated granules (Dan, 1954; Dan & Dan, 1940; Dan, Dan, & Yanagita, 1938), suggests that sea urchin embryos also exhibit patterned relaxation during ring constriction. However, rather than being confined to the pole as it is in the *C. elegans* embryo, compression of the equatorial cortex is coupled to a wave of cortical expansion that initiates at the poles and propagates through to the region adjacent to the furrow (Dan et al., 1938; Dan & Ono, 1954; Dan, Yanagita, & Sugiyama, 1937; Swann & Mitchison, 1958), a result recently confirmed by experiments employing a probe that binds lipid rafts (Gudejko et al., 2012). Cortical compression and expansion have not been mapped in vertebrate cells; however, monitoring of fluorescent latex spheres adhered to cell surface proteins (Fishkind et al., 1996; Wang et al., 1994), injected stabilized fluorescent actin filaments (Cao & Wang, 1990), and fluorescently labeled myosin II (DeBiasio et al., 1996) have all revealed concerted cortical flow towards the division plane in the equatorial region of the cell that contrasted with random surface movements at the cell poles, suggesting a pattern similar to the one we describe here for the *C. elegans* embryo.

The CoFFee model as a tool to dissect the consequences of molecular perturbations

The ability to analyze the effects of mutations and other molecular perturbations is essential to defining molecular mechanisms. The exponential accumulation of contractile ring components during constriction due to positive feedback means that the properties of the ring (component levels and constriction rate) are continuously changing. The existence of the feedback loop can also to somewhat counterintuitive results—for example, perturbations that increase the difficulty of ring constriction delay constriction onset rather than slowing constriction kinetics. Deconvolving the phenotypes observed following specific perturbations therefore poses a significant challenge. To address this challenge, we generated a straightforward analytical mathematical formulation (the CoFFee model) consisting of three differential equations and three parameters that reflect the empirical properties of the ring and cortex. In addition to describing the processes underlying the evolution of the contractile ring, the CoFFee model

428 provides a simple framework for analyzing experimental data. As we demonstrate here for rho kinase
429 depletion, assessing the effects of a perturbation on model parameters provides insights into the
430 underlying mechanistic effects of the perturbation. For example, the analysis of rho kinase depleted
431 embryos suggests that reducing the concentration of cortical myosin leads to a compensatory increase in
432 cortical flow that restores ring myosin to control levels—we note that the reason for this compensation is
433 a fascinating topic for future work. Since the CoFFee model encapsulates experimental data to
434 accurately describe the dynamics of the contractile ring and associated cortical network, an additional
435 interesting future direction will be to use parameter changes derived from the CoFFee model as input for
436 a finite-element model (similar to (Turlier et al., 2014)) in order to predict the evolution of cell shape given
437 an *a priori* knowledge of cortical and contractile ring dynamics.
438

439 **METHODS**

440 ***C. elegans strains used in this study***

Strain Name	Genotype	Reference
OD821	*ltSi200[pOD1997; Pnmy-2::nmy-2::gfp; cb-unc-119(+)] II; unc-119(ed3) III*	This study
OD857	*ltSi200[pOD1997; Pnmy-2::nmy-2::gfp; cb-unc-119(+)] II; unc-119(ed3); ruIs32[pAZ132; pie-1/GFP::histone H2B] III*	This study
OD858	*ltSi803[pOD1998; Parx-7::GFP::arx-7; cb-unc-119(+)] II; unc-119(ed3) III;*	This study
LP162	*nmy-2(cp13[nmy-2::gfp + LoxP]) I*	(Dickinson et al., 2013)
OD95	*unc-119(ed3) III; ltIs37 [pAA64; Ppie-1::mCherry::his-58; unc-119(+)] IV; ltIs38 [pAA1; Ppie-1::GFP::PH(PLC1delta1); unc-119 (+)]*	(Essex, Dammermann, Lewellyn, Oegema, & Desai, 2009)
OD3011	*ltSi1123[pSG017; Pani-1::GFP::ani-1 RE-encoded-exon5::ani-1 3'-UTR; cb unc-119(+)]II;unc-119(ed3)III*	This study
GOU2047	*cas607[arx-2::gfp knock-in] V*	(Zhu et al., 2016)

441

442 The *C. elegans* strains listed in the table were maintained at 20°C using standard methods. OD821
443 and OD858, expressing NMY-2::GFP, GFP::anillin, and GFP::ARX-7 were generated using a
444 transposon-based strategy (MosSCI; (Frokjaer-Jensen et al., 2008)). Genomic regions encoding *nmy-2*
445 (including 2079 bp and 1317 bp up and downstream of the stop codon, respectively), *ani-1* (including
446 2015 bp and 1215 bp up and downstream of the stop codon), and *arx-7* (including 3056 bp and 634 bp
447 up and downstream of the stop codon) were cloned into pCFJ151 and sequences encoding GFP were
448 inserted either just before (*nmy-2*) or after (*arx-7* and *ani-1*) the start codon. The single copy *nmy-2*
449 transgene was generated by injecting a mixture of repairing plasmid (pOD1997, 50ng/μL), transposase
450 plasmid (pJL43.1, Pglh-2::Mos2 transposase, 50ng/μL), and fluorescence selection markers (pGH8,
451 Prab-3::mCherry neuronal, 10ng/μL; pCFJ90, Pmyo-2::mCherry pharyngeal, 2.5ng/μL; pCFJ104, Pmyo-
452 3::mCherry body wall, 5ng/μL) into EG6429 (ttTi5605, Chr II). Single copy *ani-1* and *arx-7* transgenes
453 were generated by injecting a mixture of repairing plasmid (pSG017 (*ani-1*) or pOD1998 (*arx-7*),
454 50ng/μL), transposase plasmid (CFJ601, Peft-3::Mos1 transposase, 50ng/μL), selection markers (same
455 as for *nmy-2* strain) and an additional negative selection marker (pMA122; Phsp-16.41::peel-1, 10ng/μL)

456 into EG6429 (ttTi5605, Chr II). After one week, progeny of injected worms were heat-shocked at 34°C for
457 2-4 hours to induce PEEL-1 expression and kill extra chromosomal array containing worms (Seidel et al.,
458 2011). Moving worms without fluorescent markers were identified and transgene integration was
459 confirmed in their progeny by PCR spanning both homology regions in all strains.
460

461 **C. elegans *RNA-mediated interference***

Gene	Oligonucleotide 1	Oligonucleotide 2	Template	mg/ ml
arx-2 (K07C5.1)	TAATACGACTCACTA TAGGTCAGCTTCGTC AAATGCTTG	AATTAACCCTCACTA AAGGTGCAATACGC GATCCAAATA	N2 DNA	1.7
let-502 (C10H11.9)	TAATACGACTCACTA TAGGCAGCGATCGT CTGCTTATCA	AATTAACCCTCACTA AAGGTGGCTGTCGA GTTACGAATG	N2 DNA	1.9

462
463 Single-stranded RNAs (ssRNAs) were synthesized in 50µL T3 and T7 reactions (MEGAscript,
464 Invitrogen, Carlsbad, CA) using cleaned DNA templates generated by PCR from N2 DNA using the
465 oligos in the table above. Reactions were cleaned using the MEGAclear kit (Invitrogen, Carlsbad, CA),
466 and the 50 µL T3 and T7 reactions were mixed with 50µL of 3× soaking buffer (32.7mM Na_2HPO_4,
467 16.5mM KH_2PO_4, 6.3mM NaCl, 14.1mM NH_4Cl), denatured at 68°C for 10min, and then annealed at
468 37°C for 30 min to generate dsRNA. L4 hermaphrodite worms were injected with dsRNA and allowed to
469 recover at 16°C for 44-50 hours prior to imaging.
470

471 ***Monitoring cortical flow***

472 Cortical flow was monitored in images of the cortical surface in embryos expressing myosin::GFP
473 obtained from adult hermaphrodites by dissection. Embryos were mounted followed by sealing with a
474 coverslip on double thick (1 mm) low percentage agarose (0.5%) pads to prevent compression that
475 biases the initial angle of furrow ingression (**Figure 1 – Figure Supplement 2**). Images were acquired on
476 an inverted microscope (Axio Observer.Z1; Carl Zeiss) equipped with a spinning-disk confocal head
477 (CSU-X1; Yokogawa) and a 63× 1.40 NA Plan Apochromat lens (Zeiss) using a Hamamatsu Orca-ER
478 digital camera (Model C4742-95-12ERG, Hamamatsu photonics). Images were collected using custom
479 software, written in Python, that utilizes the Micro-Manager (open source software, (Edelstein et al.,

480 2014)) microscope control library. A 3 x 0.75 μm z-series was collected (400ms exposure, 10-20% laser
481 power) every 2s. After 15 time points, a 15 x 1μm z-stack, offset by 3μm from the cortical surface, was
482 imaged to monitor the position of the closing contractile ring. The entire imaging series was repeated
483 every 36s until the end of cytokinesis. Cortical flow was measured in maximum intensity projections of
484 the 3 x 0.75μm z-stacks of the cortical surface, after orientation of the images to place the embryo
485 anterior at the top and the posterior at the bottom, by correlating myosin fluorescence between
486 consecutive images using Gunnar Farnebäck's algorithm (Farnebäck, 2003) implemented within the
487 openCV library with a 30-pixel window size. The threshold was calculated for every image by maximizing
488 the ratio of total intensity inside a 200x350 pixel box positioned in the center of the embryo to the total
489 intensity outside that box.
490
491 ***Measurement of contractile ring position and size***
492 Automated methods were employed to identify the edges of the embryo, determine the position of
493 the contractile ring, and reconstruct the rings for each time point in an end-on view to determine the initial
494 ingression axis (**Figure 1 – Figure Supplement 3**). Ring size and position were determined using
495 custom Python software that: (1) identifies the orientation of the anterior-posterior (AP) axis and rotates
496 the embryo to place the embryo anterior at the top and the embryo posterior at the bottom, (2) finds the
497 embryo center in different x-z planes along the AP axis and calculates embryo radius, and (3) calculates
498 the radius of the contractile ring and determines its position within the division plane. Details of each step
499 are outlined below.
500 <u>Orienting embryos with their anterior end to the top:</u> Acquired z-plane images were convolved with a
501 10-pixel Gaussian kernel to reduce noise. An optimal signal threshold that partitioned the embryo interior
502 from exterior was identified by finding a local minimum in the intensity histogram that produced a binary
503 mask with expected area (~120000±50000 pixel^2). The orientation of the AP axis was identified by fitting
504 an ellipse to the thresholded area in the middle plane of the z stack. The anterior side was identified by
505 higher cortical myosin fluorescence and all images were rotated to place the embryo anterior at the top of
506 the image and the embryo posterior at the bottom.

507 Defining the central axis of embryo and determining embryo width: The central axis of the embryo
508 was defined by drawing a horizontal line across the oriented embryo at the midpoint between its anterior
509 and posterior ends and identifying the first and last points along this line with signal above the threshold
510 for each z-plane. The identified pixels were virtually projected in an end-on (x-z) view and fit to a circle by
511 minimizing residuals. To account for fluctuations in the embryo boundary due to noise and fluorescence
512 variation, the procedure was repeated 9 more times after shifting the position of the horizontal line
513 towards the anterior pole by 10 pixels, covering approximately 1/5 of the embryo length (500 pixels). The
514 position of the AP axis and the radius of the embryo were determined by averaging the 10
515 measurements.

516 Measuring contractile ring size and position: As illustrated for the central plane images shown in
517 Figure 1 – Figure Supplement 3, the position of the contractile ring was determined by identifying pairs of
518 points with the highest myosin fluorescence intensity on the opposite edges of the embryo in each z-
519 plane that were not more than 20 pixels apart in the horizontal direction and were located at a y-axis
520 position near the embryo middle. Contractile ring radius and position were determined by projecting the
521 points to generate an end-on (x-z) view and fitting the data with a circle. The ring fit was iteratively
522 improved by calculating predicted positions of myosin fluorescence at the ring in each z-plane using
523 initially fitted parameters. Intensity maxima within 5 pixels of the predicted location were identified and
524 the ring was refit. The initial guesses for the contractile ring size and position at the next time point were
525 estimated from the previously calculated ring values. The algorithm restricted ring position fluctuations to
526 20 pixels along anterior-posterior axis and the size was estimated assuming constant rate of ring
527 constriction. The automatic ring measurements were manually confirmed for each embryo. The initial
528 ingression axis was determined as illustrated (**Figure 1 – Figure Supplement 3**) by fitting a line through
529 the centers of the rings with a normalized ring size ($\bar{R} := R/R_{emb}$) > 0.3.

530

531 ***Embryo time alignment for averaging***

532 Sequences from individual embryos were time aligned by defining zero time (t_0) and the total time
533 of cytokinesis (t_{CK}) for each embryo, and normalizing time by t_{CK} prior to averaging, $\hat{t} := \frac{t-t_0}{t_{CK}}$. An initial

534 determination of t_0 and t_{CK} was made by fitting a line to the plot of normalized ring size ($\bar{R}(t) \coloneqq R/R_{emb}$)
535 versus time between 30% and 80% closure for each embryo as outlined in Figure 1a. Extrapolation of
536 this line for each embryo defined t_0 as the time where the fitted line intersects 1, and the time of
537 cytokinesis, t_{CK} as the time where the fitted line intersects 0. Due to the small number of measurements
538 from each embryo available for fitting (3-5 values where 0.8> $\bar{R}$ >0.3), the values of t_0 and t_{CK} were
539 refined by fitting $\bar{R}(\hat{t})$ for each embryo to the average dimensionless ring size, $< \bar{R} > (\hat{t})$. Calculation of
540 the average dimensionless ring size was performed in iterative manner. The time for each embryo was
541 aligned by t_0 and normalized by t_{CK} using estimates from the fitted line in the first iteration. The average
542 dimensionless ring size ($< \bar{R} > (\hat{t})$) was calculated by averaging normalized ring sizes of all embryos at
543 corresponding normalized time. Contractile ring size was approximated for intermediate time points by
544 linear interpolation. In further iterations, t_0 and t_{CK} were refined for every embryo by minimizing the
545 residuals between its normalized ring size, $\bar{R}(\hat{t})$, and the average dimensionless ring size, $< \bar{R} > (\hat{t})$,
546 throughout the entire timecourse of cytokinesis, thus increasing the number of time points available for
547 fitting t_0 and t_{CK} (6-10 values per embryo). After refining time alignment and normalization for each
548 embryo, average dimensionless ring size was re-calculated and t_0 and t_{CK} were refined for each embryo
549 again. The refinement process was repeated until changes in average dimensionless ring size, $< \bar{R} >$
550 $(\hat{t})$, were smaller than 0.001 on average (achieved within a few iterations). The collective fitting of all t_0
551 and t_{CK} at every iteration was performed under restriction that the line fit through $< \bar{R} > (\hat{t})$ between 0.8
552 and 0.3 intercepted 0 at $\hat{t} = 0$ and 1 at $\hat{t} = 1$. This restriction ensured that t_0 and t_{CK} determined from fits
553 of individual embryos to the average ring size would be consistent with their original definition. The
554 dimensional ring kinetics, $< R > (t)$, can be recovered using the following equation

$$< R > (t) = < R_{emb} >< \bar{R} > (\hat{t} < t_{CK} >), \quad (9)$$

555 where $< R_{emb} >= 14.7 \pm 0.7\ \mu m$ and $< t_{CK} >= 200\ \pm 30\ s$ are average embryo radius and time of
556 cytokinesis accordingly.

557
558 ***Cortical flow averaging***

559 Cortical flow averaging was performed after spatial and temporal alignment of data collected in
560 different embryos (n=93 embryos from 93 worms filmed over the course of 5 days for control, **Video 2**;
561 n=68 embryos from 68 worms filmed over the course of 4 days for *arx-2(RNAi)*, **Video 3**). The number of
562 embryos was chosen to achieve at least 10-fold coverage for all areas of the cortical map for controls
563 and 5-fold coverage for *arx-2(RNAi)*. Linear interpolation was used to approximate the flow between
564 consecutive time points. Because our imaging regime required periodic z-stack acquisition to determine
565 the trajectory of ring closure, no flow approximation was done during those time periods (~6s gap every
566 30s). The flow data for each time point was represented as a set of vectors with direction and magnitude
567 corresponding to the direction and magnitude of the cortical flow at the base of the vector. The base of
568 each vector had two spatial coordinates: x, the position along the anterior-posterior axis (where the
569 position of the contractile ring was defined as 0), and θ, the angular position relative to the initial
570 ingression axis (defined as described in **Figure 1A and Figure 1 – Figure Supplement 3**). We note that
571 mitotic exit is accompanied by a brief (~50-60s) period of rotational flow ((Naganathan, Furthauer,
572 Nishikawa, Julicher, & Grill, 2014; Schonegg, Hyman, & Wood, 2014); see **Video 1;**), which dissipates
573 soon after initiation of cytokinesis (~$\hat{t}$=0.2-0.3). As this rotational contribution is not relevant here, we
574 removed it by averaging the data from the right and left halves of the embryo (in an end-on view),
575 allowing us to focus on rotation-independent flows. Thus the flow with angular positions greater than 180
576 degrees was mirrored in angular direction

$$f_\theta(\hat{t}, x, \theta > 180) \;\rightarrow\; -f_\theta(\hat{t}, x, 360 - \theta), \tag{10}$$

577 f_θ is the angular component of the flow vector $\vec{f}$. The flows were normalized by the embryo size and
578 cytokinesis rate $\vec{\bar{f}}(\hat{t}, x, \theta) \coloneqq \frac{t_{CK}}{R_{emb}} \vec{f}(\hat{t}, x, \theta)$ and averaged according to its position and time

$$< \vec{\bar{f}} > (\hat{t}, x, \theta) = \frac{\sum_{emb} \vec{\bar{f}}(\hat{t}, x, \theta)}{N_{emb}}. \tag{11}$$

579

580 ***Calculation of expected cortical surface flow profiles***

581 To aid in the interpretation of experimental results, expected profiles for cortical surface movement were
582 calculated for defined patterns of cortical surface increase and plotted (**Figure 1B and Figure 1 – Figure**
583 **Supplement 5**). The general form of surface movement velocity is given by the following equation

$$v(x) = \int_0^x g(x')dx' + u, \tag{12}$$

584 where $g(x)$ is the amount surface gain and u is the velocity of asymmetric ring movement, which could
585 be positive or negative, depending on whether the ring is moving towards or away from the surface.
586 From equation (12) we obtain the following predictions

587 Uniform surface increase: $v(x) = Cx + u$;

588 Polar surface increase: $v(x) = C + u$;

589 Behind the ring surface increase: $v(x) = u$ (if the asymmetry of cytokinetic furrowing arises due to
590 global surface movement) or $v(x) = 0$ (if the asymmetry in surface increase is related to the asymmetric
591 furrowing).

592

593 ***Cortical laser ablation***

594 Cortical laser ablations, presented in Figure 2, were performed using a robotic laser microscope
595 system (RoboLase) (Botvinick & Berns, 2005). Embryos expressing myosin::GFP were mounted using
596 standard procedures. A cortical cut, approximately 10 μm long, was made on the anterior side of the
597 embryo when the ring was at ~50% closure (7μm radius). The cut was confirmed by comparison of
598 cortical fluorescence images before and after the cut and was considered successful if the foci moved
599 away from the cut area (~3.5μm distance), indicating cortical tension release. Contractile ring closure
600 rate was calculated by measuring the difference in ring sizes before and after the cut, assessed from two
601 4x2μm z-stacks acquired immediately before the cut and 13s later. Errors in measuring the radius at the
602 two timepoints were determined from the procedure used to fit the data to a circle and were propagated
603 to determine the errors in the constriction rate measurements for individual embryos; mean errors are
604 S.E.M. The cortical opening after ablation was approximately 35μm^2; this translates into an additional
605 reduction in ring radius by ~0.8μm, if the cortical surface tension dominates the ring closure rate. This
606 additional decrease in ring size within 13s should correspond to increase of the control rate (0.22μm/s)

607 by ~30% (0.06μm/s). The experiment was repeated 19 times for no cut condition, 14 times for parallel
608 cut, and 15 times for perpendicular cut. All imaging was performed over the course of 5 days. The
609 number of embryos was chosen to achieve sufficient accuracy in the determination of mean ring closure
610 rates to assess whether it was altered by the cuts.
611

612 ***Calculation of the surface area flowing into the division plane***

613 We calculated the amount of surface area flowing into the division plane from flow measurements
614 made 7 μm away from the position of the furrow on the anterior and posterior sides (as illustrated in
615 **Figure 3A**). The rate of the surface flow is

$$\frac{dA_{surf}}{d\hat{t}}(\hat{t}) = 2R_{emb}\int_0^{\pi} < \vec{f} > (\hat{t}, x_0, \theta)d\theta \ , \tag{13}$$

616 where x_0 is -7 μm and 7 μm for the rate of flow from the anterior or the posterior sides, respectively. The
617 total amount of surface area that entered the division plane from any time $\bar{t}_0$ to $\bar{t}$ is obtained by
618 integrating equation (13) over time

$$A_{surf}(\hat{t}) = \int_{\hat{t}_0}^{\hat{t}} \frac{dA_{surf}}{d\hat{t}}\bigg|_{ant} + \frac{dA_{surf}}{d\hat{t}}\bigg|_{post}(t')dt'. \tag{14}$$

619 The increase in area of the division plane was calculated as following

$$A_{div\ plane}(\hat{t}) = 2\pi(< R >^2 (\hat{t}_0) - < R >^2 (\hat{t})). \tag{15}$$

620 In Figure 3A we used $\hat{t}_0 = -0.2$. The extra cortex delivered into the ring can be inferred from the
621 difference between the surface area entering the division plane and the area of the division plane

$$A_{flow}(\hat{t}) := A_{surf}(\hat{t}) - A_{div\ plane}(\hat{t}). \tag{16}$$

622

623 ***Division plane imaging***

624 For quantification of myosin::GFP and GFP::anillin amounts in the contractile ring, adult worm
625 dissection and one-cell stage embryos imaging was performed in a custom microdevice (Carvalho et al.,
626 2011). The device was mounted on an inverted microscope (Axio Observer.Z1; Carl Zeiss) and embryos
627 were imaged with a 63x1.4NA Plan Apochromat objective using an electron-multiplying charge-coupled

628 device camera (QuantEM:512SC, Photometrics; 100ms exposure, EM gain set to 500, 10% laser
629 power). Division planes were reconstructed from 40 x 0.5μm z-stacks collected every 30s after
630 background subtraction and attenuation correction. All imaging was done at 20°C.
631
632 ***Contractile ring photo-bleaching and imaging***
633 1-cell stage embryos were mounted in microdevices as for division plane imaging and 4-cell stage
634 embryos were mounted on slides with 2% agarose pads. Embryos were imaged on a Nikon TE2000-E
635 inverted microscope equipped with a 60x1.40NA objective, an EM-CCD camera (iXon; Andor
636 Technology; EM-Gain=220, Exposure =100ms), and a krypton-argon 2.5 W water-cooled laser. For 1-cell
637 stage embryos, division planes were reconstructed from 30x1μm stacks acquired every 20s with 20%
638 laser power and photo-bleaching was performed by 2 sweeps of a 488nm laser with 100% power and
639 500μs dwell time. For 4-cell stage embryos, division planes were reconstructed from 16x1μm stacks
640 acquired every 10s with 50% laser power and photo-bleaching was performed by 2 sweeps of a 488nm
641 laser with 100% power and 100μs dwell time. For 4-cell stage embryos, the time between the
642 prebleached and first postbleached images was 6s.
643
644 ***Estimation of depth attenuation***
645 To estimate depth attenuation within the division plane, we quantified the intensity of the division
646 plane in two cell embryos expressing a GFP-tagged probe expected to be uniformly present on the
647 plasma membrane. From each image, we subtracted a background intensity calculated as the average
648 value inside two 4x4 μm rectangles positioned 2 μm away from the division plane inside the anterior and
649 posterior cells. The division plane intensity profile was obtained by performing a 30 pixel maximum
650 intensity projection along the AP axis, with the division plane positioned approximately in the middle
651 (**Figure 3 – Figure Supplement 4**). The intensity profiles in z from 13 embryos were fitted to an
652 exponential using the same characteristic attenuation depth for all embryos

$$I = I_0 e^{-z/z_{att}}, \tag{17}$$

653 which yielded a characteristic depth of attenuation, z_{att}, of 15 μm.

654

655 ***Quantification of myosin and anillin intensity in the contractile ring and on the cortex***

656 For embryos at the 1-cell stage, myosin::GFP and GFP::anillin intensities in the contractile ring and
657 on the cortex were quantified in 40x0.5 μm z-stacks containing the ring after correction for depth
658 attenuation and subtraction of background fluorescence. Average intensity along the ring was calculated
659 across a set of embryos in 30 degree arcs (for myosin::GFP, n=36 embryos from 18 worms filmed over 5
660 days for controls and 24 embryos from 15 worms filmed over 5 days for *let-502(RNAi)*; for anillin::GFP,
661 n= 26 embryos from 14 worms filmed over 4 days and 30 embryos from 18 worms filmed over the course
662 of 4 days for *let-502(RNAi)*). The number of embryos was chosen to determine mean fluorescence with
663 sufficient accuracy to derive appropriate conclusions. Positions along the ring were referenced based on
664 the angle between the line from the position on the ring to the ring center and the initial ingression axis.
665 Linear interpolation in time was used for every embryo to estimate intensity in the intermediate time
666 points to perform averaging. Measured intensities were divided by arc length and averaged between
667 different embryos to obtain mean GFP fluorescence per unit length for different angular ranges and the
668 average for all angles. Total ring GFP fluorescence was calculated by integrating over ring perimeter.
669 Cortical intensities were quantified by choosing the time point with the ring size closest to $\bar{R} = 0.8$ and
670 measuring total fluorescence in the 15th plane after correction for depth attenuation and subtraction of
671 background fluorescence.

672 Measurements of myosin::GFP fluorescence in the ring at the 4-cell stage were performed as
673 described in Carvalho et. al., 2009. However background fluorescence was determined as the mean
674 fluorescence within a variable size circle at least 10 pixels in diameter, instead of fixed at 10 pixels, to
675 improve measurement quality.

676

677 ***Derivation of the Cortical Flow Feedback (CoFFee) model for cytokinesis***

678 The CoFFee model formalizes the following conceptual view of cytokinesis: Active RhoA recruits
679 contractile ring components to the equatorial cortex, where myosin engages with actin to exert an
680 isotropic force that compresses the underlying cortex. Polar relaxation releases tension in the direction
681 perpendicular to the ring, but not in the around-the-ring direction, generating anisotropic boundary

conditions that cause the system to exhibit distinct behavior in the two directions. Disassembly in the around-the-ring direction reduces ring components in proportion to the reduction in length, and does not alter the per unit length amount of myosin. Thus, changes in myosin levels are determined solely by ring-directed cortical flow along the direction perpendicular to the ring, which can be solved as a one-dimensional problem. We assume that the cortical compression rate (between x and $x + dx$) is proportional to local myosin concentration, $m(x,t)$, which exerts stress onto the actin network resulting in

$$\frac{\delta\varepsilon}{\delta t}(x,t) = -\alpha m(x,t), \tag{18}$$

where ε is the cortical strain (i.e. change in length of cortical surface per unit length) and α is a proportionality constant that reflects the ability of the cortex to be compressed by ring myosin. The velocity of cortical surface movement is obtained from the following relationship (see also equation (12)).

$$v(x,t) = \int_0^x \frac{\delta\varepsilon}{\delta t}(x',t)dx'. \tag{19}$$

The conservation of mass for myosin flow results in the following

$$\frac{\partial m}{\partial t}(x,t) = -\frac{\partial}{\partial x}\big(m(x,t)v(x,t)\big) = \frac{\partial}{\partial x}(m(x,t)\int_0^x \alpha m(x',t)dx'). \tag{20}$$

If we integrate equation (20) over *x* on *(-w, w)* domain we obtain

$$dM_{ring}(t)/dt = \alpha m_{cort} M_{ring}(t), \tag{21}$$

where $M_{ring}(t) \coloneqq \int_{-w}^{w} m(x,t)dx$ is the total per unit length amount of engaged ring myosin, $2w$ is the width of the contractile ring/active zone where myosin is engaged and compressing cortex and $m_{cort} \coloneqq m(w,t)$ is the concentration of myosin on the cortex delivered into the contractile ring. The velocity of ring-directed cortical flow is

$$v_{flow}(t) = \alpha M_{ring}(t)/2, \tag{22}$$

The one half is included to account for the fact that flow comes in from both sides. The solution of equation (21) is

$$M_{ring}(t) = M_{0\,ring}\, e^{t/\tau}, \tag{23}$$

where we define the characteristic time of myosin accumulation, τ, as $\frac{1}{\alpha m_{cort}}$. Note that the total amount of myosin in the ring will be the amount of engaged myosin plus an added baseline that would include any myosin not involved in compression (see equation (5)). We assume the rate of ring shrinkage is proportional to the amount of ring myosin, as observed in our data,

$$\frac{1}{R}\frac{dR}{dt} = -\beta M_{ring}(t), \tag{24}$$

where β is a proportionality coefficient that reflects the ability of the ring to be constricted by ring myosin. Using equations (23) and (24), we obtain the dynamics of contractile ring size over time

$$\bar{R}(t) = \bar{R}_{ini} e^{-\beta\tau M_{0\,ring}\exp(t/\tau)}, \tag{25}$$

where $\bar{R}_{ini}$ is the dimensionless characteristic size of the ring; essentially the radius at minus infinity if the same exponential process controlling contractile ring assembly extended back in time infinitely. Instead, *in vivo* cytokinesis initiates when spindle-based signaling activates RhoA on the equatorial cortex leading to the abrupt recruitment of contractile ring components. If the time frame of reference is chosen so that $t = 0$ is cytokinesis onset immediately following the initial patterning of the cortex by RhoA, $M_{0\,ring}$ is the amount of ring myosin immediately following this event and the initial size of the ring is

$$\bar{R}_0(t) = \bar{R}_{ini} e^{-\beta\tau M_{0\,ring}}. \tag{26}$$

To compare our model with data we use the time frame of reference where $t = 0$ is the point of 50% closure (i.e. $\bar{R}(t = 0) = \frac{1}{2}$). In this reference, $M_{0\,ring} = \frac{\ln(\bar{R}_{ini})}{\beta\tau}$, and by defining dimensionless velocity as $\bar{v} := \tau v$, we obtain equations (4-8). Note that equation (4) can be rewritten in the following way

$$\bar{R}(\bar{t}) = \bar{R}_{ini} e^{-\frac{1}{\bar{R}}\frac{d\bar{R}}{d\bar{t}}}, \tag{27}$$

where $\bar{t} := t/\tau$. This relationship implies that in this dimensionless time, where $\bar{R}(\bar{t} = 0) = \frac{1}{2}$, any two rings of the same size have the same dimensionless constriction rate.

Data availability

All data is available from the authors upon request.

719 ***Code availability***

720 The custom computer code used in this study is freely available from the authors upon request.

721

722 **ACKNOWLEDGEMENTS**

723 This work was supported by a fellowship from the Jane Coffin Childs Memorial Fund to R.N.K. and
724 grants to M.W.B from AFOSR (FA9550-08-1-0284) and the Beckman Laser Institute Foundation. J.S.G-
725 C was supported by the University of California, San Diego Cancer Cell Biology Training Program (T32
726 CA067754). A.D. and K.O. receive salary and other support from the Ludwig Institute for Cancer
727 Research.

728

REFERENCES

Biron, D., Libros, P., Sagi, D., Mirelman, D., & Moses, E. (2004). Biphasic cytokinesis and cooperative single cell re-production. In A. T. Skejeltorp & A. V. Belushkin (Eds.), *Forces, Growth and Form in Soft Condensed Matter: At the Interface between Physics and Biology* (pp. 217-234): Springer, Berlin.

Bluemink, J. G., & de Laat, S. W. (1973). New membrane formation during cytokinesis in normal and cytochalasin B-treated eggs of Xenopus laevis. I. Electron microscope observations. *J Cell Biol, 59*(1), 89-108.

Botvinick, E. L., & Berns, M. W. (2005). Internet-based robotic laser scissors and tweezers microscopy. *Microsc Res Tech, 68*(2), 65-74. doi:10.1002/jemt.20216

Bourdages, K. G., Lacroix, B., Dorn, J. F., Descovich, C. P., & Maddox, A. S. (2014). Quantitative analysis of cytokinesis in situ during C. elegans postembryonic development. *PLoS One, 9*(10), e110689. doi:10.1371/journal.pone.0110689

Byers, T. J., & Armstrong, P. B. (1986). Membrane protein redistribution during Xenopus first cleavage. *J Cell Biol, 102*(6), 2176-2184.

Calvert, M. E., Wright, G. D., Leong, F. Y., Chiam, K. H., Chen, Y., Jedd, G., & Balasubramanian, M. K. (2011). Myosin concentration underlies cell size-dependent scalability of actomyosin ring constriction. *J Cell Biol, 195*(5), 799-813. doi:10.1083/jcb.201101055

Canman, J. C., Hoffman, D. B., & Salmon, E. D. (2000). The role of pre- and post-anaphase microtubules in the cytokinesis phase of the cell cycle. *Curr Biol, 10*(10), 611-614.

Cao, L. G., & Wang, Y. L. (1990). Mechanism of the formation of contractile ring in dividing cultured animal cells. II. Cortical movement of microinjected actin filaments. *J Cell Biol, 111*(5 Pt 1), 1905-1911.

Carvalho, A., Desai, A., & Oegema, K. (2009). Structural memory in the contractile ring makes the duration of cytokinesis independent of cell size. *Cell, 137*(5), 926-937. doi:10.1016/j.cell.2009.03.021

Carvalho, A., Olson, S. K., Gutierrez, E., Zhang, K., Noble, L. B., Zanin, E., . . . Oegema, K. (2011). Acute drug treatment in the early C. elegans embryo. *PLoS One, 6*(9), e24656. doi:10.1371/journal.pone.0024656

Chaudhuri, O., Parekh, S. H., & Fletcher, D. A. (2007). Reversible stress softening of actin networks. *Nature, 445*(7125), 295-298. doi:10.1038/nature05459

Dan, K. (1954). The cortical movement in Arbacia Punctulata eggs through cleavage cycles. *Embryologia, 2*(12), 115-122.

Dan, K., & Dan, J. C. (1940). Behavior of the Cell Surface during Cleavage: III. On the formation of New Surface in the Eggs of Strongylocentrotus Pulcherrimus. *Biological Bulletin, 78*(3), 486-501.

Dan, K., Dan, J. C., & Yanagita, T. (1938). Behaviour of the Cell Surface During Cleavage. II. *Cytologia, 8*, 521-531.

Dan, K., & Ono, T. (1954). A method of computation of the surface area of the cell. *Embryologia, 2*, 87-98.

Dan, K., Yanagita, T., & Sugiyama, M. (1937). Behavior of the cell surface during cleavage. I. *Protoplasma, 28*, 68-81.

Danilchik, M. V., Bedrick, S. D., Brown, E. E., & Ray, K. (2003). Furrow microtubules and localized exocytosis in cleaving Xenopus laevis embryos. *J Cell Sci, 116*(Pt 2), 273-283.

Davies, T., Jordan, S. N., Chand, V., Sees, J. A., Laband, K., Carvalho, A. X., . . . Canman, J. C. (2014). High-resolution temporal analysis reveals a functional timeline for the molecular regulation of cytokinesis. *Dev Cell, 30*(2), 209-223. doi:10.1016/j.devcel.2014.05.009

DeBiasio, R. L., LaRocca, G. M., Post, P. L., & Taylor, D. L. (1996). Myosin II transport, organization, and phosphorylation: evidence for cortical flow/solation-contraction coupling during cytokinesis and cell locomotion. *Mol Biol Cell, 7*(8), 1259-1282.

Dickinson, D. J., Ward, J. D., Reiner, D. J., & Goldstein, B. (2013). Engineering the Caenorhabditis elegans genome using Cas9-triggered homologous recombination. *Nat Methods, 10*(10), 1028-1034. doi:10.1038/nmeth.2641

Edelstein, A. D., Tsuchida, M. A., Amodaj, N., Pinkard, H., Vale, R. D., & Stuurman, N. (2014). Advanced methods of microscope control using muManager software. *J Biol Methods, 1*(2). doi:10.14440/jbm.2014.36

Essex, A., Dammermann, A., Lewellyn, L., Oegema, K., & Desai, A. (2009). Systematic analysis in Caenorhabditis elegans reveals that the spindle checkpoint is composed of two largely independent branches. *Mol Biol Cell, 20*(4), 1252-1267. doi:10.1091/mbc.E08-10-1047

Farnebäck, G. (2003). Two-frame motion estimation based on polynomial expansion lecture notes in computer science (pp. 363-370): Springer Science and Buisness Media.

Fededa, J. P., & Gerlich, D. W. (2012). Molecular control of animal cell cytokinesis. *Nat Cell Biol, 14*(5), 440-447. doi:10.1038/ncb2482

Fishkind, D. J., Silverman, J. D., & Wang, Y. L. (1996). Function of spindle microtubules in directing cortical movement and actin filament organization in dividing cultured cells. *J Cell Sci, 109 (Pt 8)*, 2041-2051.

Frokjaer-Jensen, C., Davis, M. W., Hopkins, C. E., Newman, B. J., Thummel, J. M., Olesen, S. P., . . . Jorgensen, E. M. (2008). Single-copy insertion of transgenes in Caenorhabditis elegans. *Nat Genet, 40*(11), 1375-1383. doi:10.1038/ng.248

Gardel, M. L., Schneider, I. C., Aratyn-Schaus, Y., & Waterman, C. M. (2010). Mechanical integration of actin and adhesion dynamics in cell migration. *Annu Rev Cell Dev Biol, 26*, 315-333. doi:10.1146/annurev.cellbio.011209.122036

Green, R. A., Paluch, E., & Oegema, K. (2012). Cytokinesis in animal cells. *Annu Rev Cell Dev Biol, 28*, 29-58. doi:10.1146/annurev-cellbio-101011-155718

Greenspan, H. P. (1978). On fluid-mechanical simulations of cell division and movement. *J Theor Biol, 70*, 125-134.

Gudejko, H. F., Alford, L. M., & Burgess, D. R. (2012). Polar expansion during cytokinesis. *Cytoskeleton (Hoboken), 69*(11), 1000-1009. doi:10.1002/cm.21078

Hickson, G. R., Echard, A., & O'Farrell, P. H. (2006). Rho-kinase controls cell shape changes during cytokinesis. *Curr Biol, 16*(4), 359-370. doi:10.1016/j.cub.2005.12.043

Hird, S. N., & White, J. G. (1993). Cortical and cytoplasmic flow polarity in early embryonic cells of Caenorhabditis elegans. *J Cell Biol, 121*(6), 1343-1355.

Jordan, S. N., & Canman, J. C. (2012). Rho GTPases in animal cell cytokinesis: an occupation by the one percent. *Cytoskeleton (Hoboken), 69*(11), 919-930. doi:10.1002/cm.21071

Ma, X., Kovacs, M., Conti, M. A., Wang, A., Zhang, Y., Sellers, J. R., & Adelstein, R. S. (2012). Nonmuscle myosin II exerts tension but does not translocate actin in vertebrate cytokinesis. *Proc Natl Acad Sci U S A, 109*(12), 4509-4514. doi:10.1073/pnas.1116268109

Mabuchi, I. (1994). Cleavage furrow: timing of emergence of contractile ring actin filaments and establishment of the contractile ring by filament bundling in sea urchin eggs. *J Cell Sci, 107 (Pt 7)*, 1853-1862.

Maddox, A. S., Lewellyn, L., Desai, A., & Oegema, K. (2007). Anillin and the septins promote asymmetric ingression of the cytokinetic furrow. *Dev Cell, 12*(5), 827-835. doi:10.1016/j.devcel.2007.02.018

Mandato, C. A., & Bement, W. M. (2003). Actomyosin transports microtubules and microtubules control actomyosin recruitment during Xenopus oocyte wound healing. *Curr Biol, 13*(13), 1096-1105.

Martineau, S. N., Andreassen, P. R., & Margolis, R. L. (1995). Delay of HeLa cell cleavage into interphase using dihydrocytochalasin B: retention of a postmitotic spindle and telophase disc correlates with synchronous cleavage recovery. *J Cell Biol, 131*(1), 191-205.

Matsumura, F. (2005). Regulation of myosin II during cytokinesis in higher eukaryotes. *Trends Cell Biol, 15*(7), 371-377. doi:10.1016/j.tcb.2005.05.004

Mayer, M., Depken, M., Bois, J. S., Julicher, F., & Grill, S. W. (2010). Anisotropies in cortical tension reveal the physical basis of polarizing cortical flows. *Nature, 467*(7315), 617-621. doi:10.1038/nature09376

Munjal, A., & Lecuit, T. (2014). Actomyosin networks and tissue morphogenesis. *Development, 141*(9), 1789-1793. doi:10.1242/dev.091645

Murrell, M., Oakes, P. W., Lenz, M., & Gardel, M. L. (2015). Forcing cells into shape: the mechanics of actomyosin contractility. *Nat Rev Mol Cell Biol, 16*(8), 486-498. doi:10.1038/nrm4012

Naganathan, S. R., Furthauer, S., Nishikawa, M., Julicher, F., & Grill, S. W. (2014). Active torque generation by the actomyosin cell cortex drives left-right symmetry breaking. *Elife, 3*, e04165. doi:10.7554/eLife.04165

Pelham, R. J., & Chang, F. (2002). Actin dynamics in the contractile ring during cytokinesis in fission yeast. *Nature, 419*(6902), 82-86. doi:10.1038/nature00999

Piekny, A., Werner, M., & Glotzer, M. (2005). Cytokinesis: welcome to the Rho zone. *Trends Cell Biol, 15*(12), 651-658. doi:10.1016/j.tcb.2005.10.006

Piekny, A. J., & Mains, P. E. (2002). Rho-binding kinase (LET-502) and myosin phosphatase (MEL-11) regulate cytokinesis in the early Caenorhabditis elegans embryo. *J Cell Sci, 115*(Pt 11), 2271-2282.

Reymann, A. C., Staniscia, F., Erzberger, A., Salbreux, G., & Grill, S. W. (2016). Cortical flow aligns actin filaments to form a furrow. *Elife, 5*. doi:10.7554/eLife.17807

Rodrigues, N. T., Lekomtsev, S., Jananji, S., Kriston-Vizi, J., Hickson, G. R., & Baum, B. (2015). Kinetochore-localized PP1-Sds22 couples chromosome segregation to polar relaxation. *Nature, 524*(7566), 489-492. doi:10.1038/nature14496

Salbreux, G., Charras, G., & Paluch, E. (2012). Actin cortex mechanics and cellular morphogenesis. *Trends Cell Biol, 22*(10), 536-545. doi:10.1016/j.tcb.2012.07.001

Schonegg, S., Hyman, A. A., & Wood, W. B. (2014). Timing and mechanism of the initial cue establishing handed left-right asymmetry in Caenorhabditis elegans embryos. *Genesis, 52*(6), 572-580.

Schroeder, T. E. (1975). Dynamics of the contractile ring. *Soc Gen Physiol Ser, 30*, 305-334.

Schroeder, T. E. (1990). The contractile ring and furrowing in dividing cells. *Ann N Y Acad Sci, 582*, 78-87.

Sedzinski, J., Biro, M., Oswald, A., Tinevez, J. Y., Salbreux, G., & Paluch, E. (2011). Polar actomyosin contractility destabilizes the position of the cytokinetic furrow. *Nature, 476*(7361), 462-466. doi:10.1038/nature10286

Seidel, H. S., Ailion, M., Li, J., van Oudenaarden, A., Rockman, M. V., & Kruglyak, L. (2011). A novel sperm-delivered toxin causes late-stage embryo lethality and transmission ratio distortion in C. elegans. *PLoS Biol, 9*(7), e1001115. doi:10.1371/journal.pbio.1001115

Selman, G. G., & Perry, M. M. (1970). Ultrastructural changes in the surface layers of the newt's egg in relation to the mechanism of its cleavage. *J Cell Sci, 6*(1), 207-227.

Straight, A. F., Cheung, A., Limouze, J., Chen, I., Westwood, N. J., Sellers, J. R., & Mitchison, T. J. (2003). Dissecting temporal and spatial control of cytokinesis with a myosin II Inhibitor. *Science, 299*(5613), 1743-1747. doi:10.1126/science.1081412

Swann, M. M., & Mitchison, J. M. (1958). Cleavage in animal cells. *Biological Reviews, 33*(1), 103-135.

Taber, L. A. (1995). Biomechanics of growth, remodeling, and morphogenesis. *Appl Mech Rev, 48*(8), 487-545.

Tseng, Y., & Wirtz, D. (2004). Dendritic branching and homogenization of actin networks mediated by arp2/3 complex. *Phys Rev Lett, 93*(25), 258104. doi:10.1103/PhysRevLett.93.258104

Turlier, H., Audoly, B., Prost, J., & Joanny, J. F. (2014). Furrow constriction in animal cell cytokinesis. *Biophys J, 106*(1), 114-123. doi:10.1016/j.bpj.2013.11.014

Vale, R. D., Spudich, J. A., & Griffis, E. R. (2009). Dynamics of myosin, microtubules, and Kinesin-6 at the cortex during cytokinesis in Drosophila S2 cells. *J Cell Biol, 186*(5), 727-738. doi:10.1083/jcb.200902083

Wang, Y. L., Silverman, J. D., & Cao, L. G. (1994). Single particle tracking of surface receptor movement during cell division. *J Cell Biol, 127*(4), 963-971.

White, J. G., & Borisy, G. G. (1983). On the mechanisms of cytokinesis in animal cells. *J Theor Biol, 101*(2), 289-316.

Wolpert, L. (1960). The mechanics and mechanism of cleavage. *International review of cytology, 10*, 163-216.

Wu, J. Q., & Pollard, T. D. (2005). Counting cytokinesis proteins globally and locally in fission yeast. *Science, 310*(5746), 310-314. doi:10.1126/science.1113230

Xiong, H., Mohler, W. A., & Soto, M. C. (2011). The branched actin nucleator Arp2/3 promotes nuclear migrations and cell polarity in the C. elegans zygote. *Dev Biol, 357*(2), 356-369. doi:10.1016/j.ydbio.2011.07.008

Yumura, S. (2001). Myosin II dynamics and cortical flow during contractile ring formation in Dictyostelium cells. *J Cell Biol, 154*(1), 137-146.

Zhou, M., & Wang, Y. L. (2008). Distinct pathways for the early recruitment of myosin II and actin to the cytokinetic furrow. *Mol Biol Cell, 19*(1), 318-326. doi:10.1091/mbc.E07-08-0783

Zhu, Z., Chai, Y., Jiang, Y., Li, W., Hu, H., Li, W., . . . Ou, G. (2016). Functional Coordination of WAVE and WASP in C. elegans Neuroblast Migration. *Dev Cell, 39*(2), 224-238. doi:10.1016/j.devcel.2016.09.029

Zinemanas, D., & Nir, A. (1987). Fluid mechanical simulations of cell furrowing due to anisotropic surface forces. In N. Akkas (Ed.), *Biomechanics of cell division* (pp. 281-305): Plenum Press, New York.

Zinemanas, D., & Nir, A. (1988). On the viscous deformation of biological cells under anisotropic surface tension. *J Fluid Mech, 193*, 217-241.

Zumdieck, A., Kruse, K., Bringmann, H., Hyman, A. A., & Julicher, F. (2007). Stress generation and filament turnover during actin ring constriction. *PLoS One, 2*(8), e696. doi:10.1371/journal.pone.0000696

FIGURES AND FIGURE LEGENDS

Figure 1

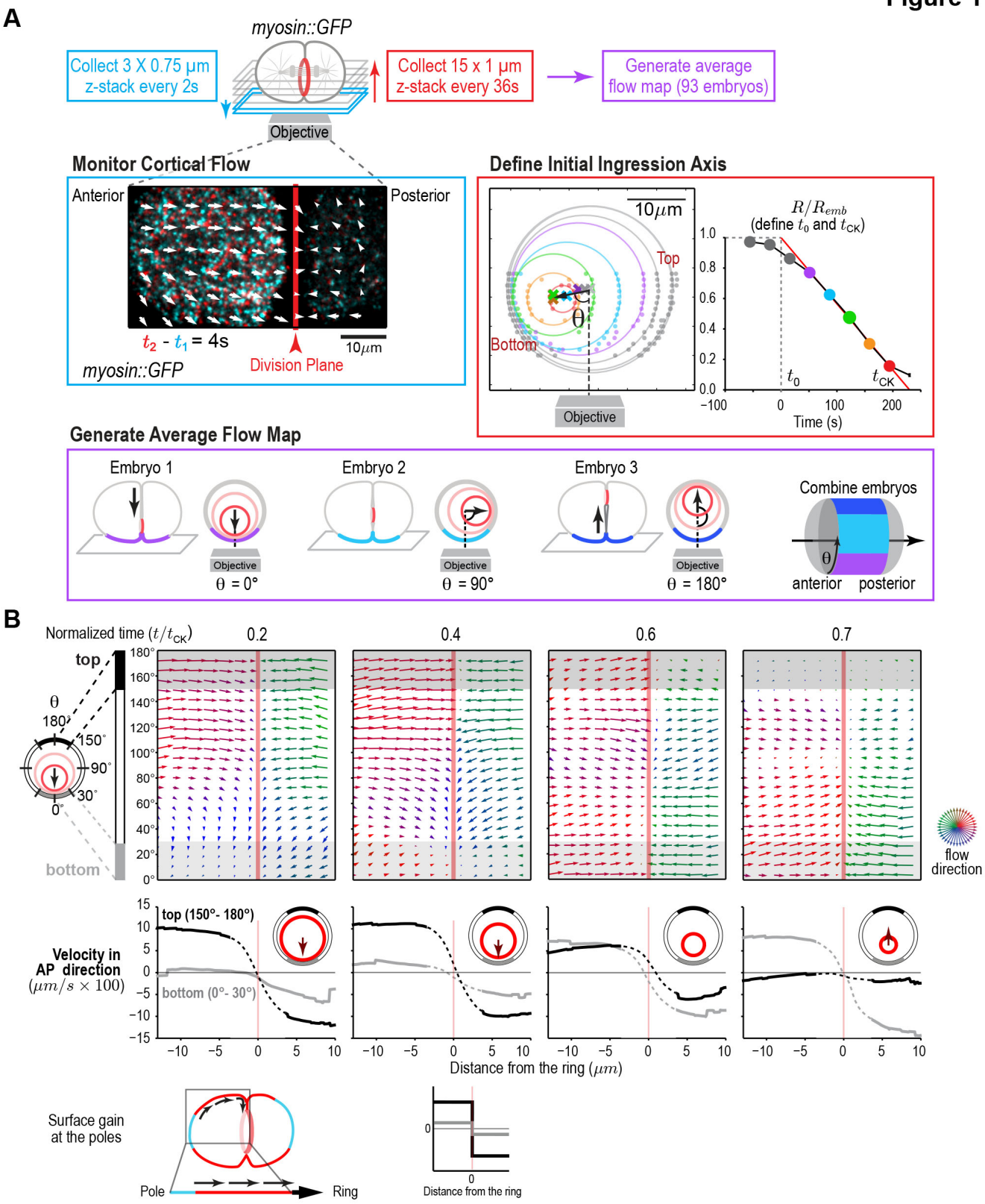

906 **Figure 1**. **An average cortical flow map reveals that surface gain occurs at the cell poles.** (**A**) (*top*)
907 Schematic of the experimental procedure. (*middle, left*) Superposition of images of the cortex acquired
908 4s apart. Arrows indicate cortical flow (magnified 2.5X). (*middle, right*) The initial ingression axis, t_0, and
909 t_{CK} were defined as shown for a representative embryo. The angle θ specifies the position of the imaged
910 cortex relative to the initial ingression axis. Image and quantification are representative of the 93 imaged
911 embryos. (*bottom*) Angular position was used to combine data from 93 embryos to generate an average
912 flow map. (**B**) (*top*) Average flow at the indicated timepoints. Arrows show direction and magnitude of the
913 displacement in 2s (magnified 20X). (*middle*) Graphs are average velocity in the A-P direction versus
914 position along the A-P axis for the cortex on the top (*black*) and bottom (*grey*) of the embryo (*shaded in*
915 *flow maps*). Surface movement changes direction across the division plane, the apparent velocity
916 gradient close to the division plane is a projection artifact due to surface curvature (dotted regions on
917 velocity curves). (*bottom*) Schematics show a one-dimensional representation and expected cortical
918 velocity plot for surface gain at the poles.
919

Figure 1—figure supplement 1

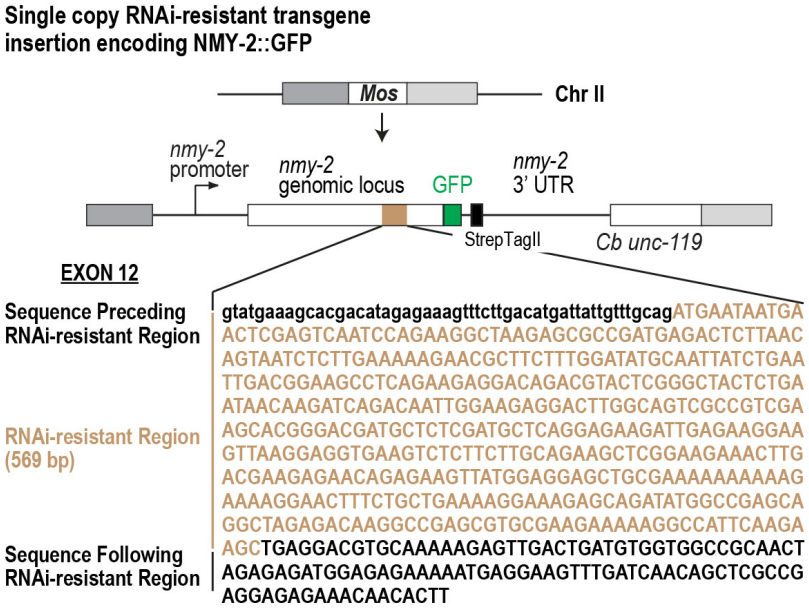

920

921 **Figure 1 – Figure Supplement 1. Schematic of the single-copy *nmy-2::gfp* transgene inserted into**
922 **a specific locus on chromosome II**. Cb *unc-119*, the *unc-119* coding region from the related nematode
923 *C. briggsae*, was used as a transformation marker. The transgene was re-encoded while maintaining
924 amino acid sequence in the indicated region to render it resistant to RNAi targeting the endogenous
925 gene for other experiments, we did not use this feature in the experiments reported here.

Figure 1—figure supplement 2

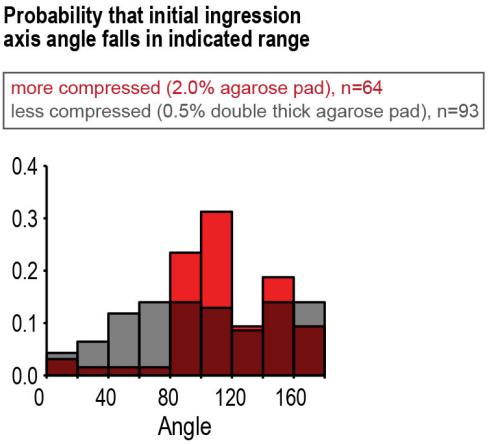

926

927 **Figure 1 – Figure Supplement 2. Compression biases the direction of contractile ring closure.**
928 Graph plotting the probability that the angle between the objective axis and the initial ingression axis falls
929 in the indicated range for embryos mounted with more *(red*) or less (*grey*) compression.
930

Figure 1—figure supplement 3

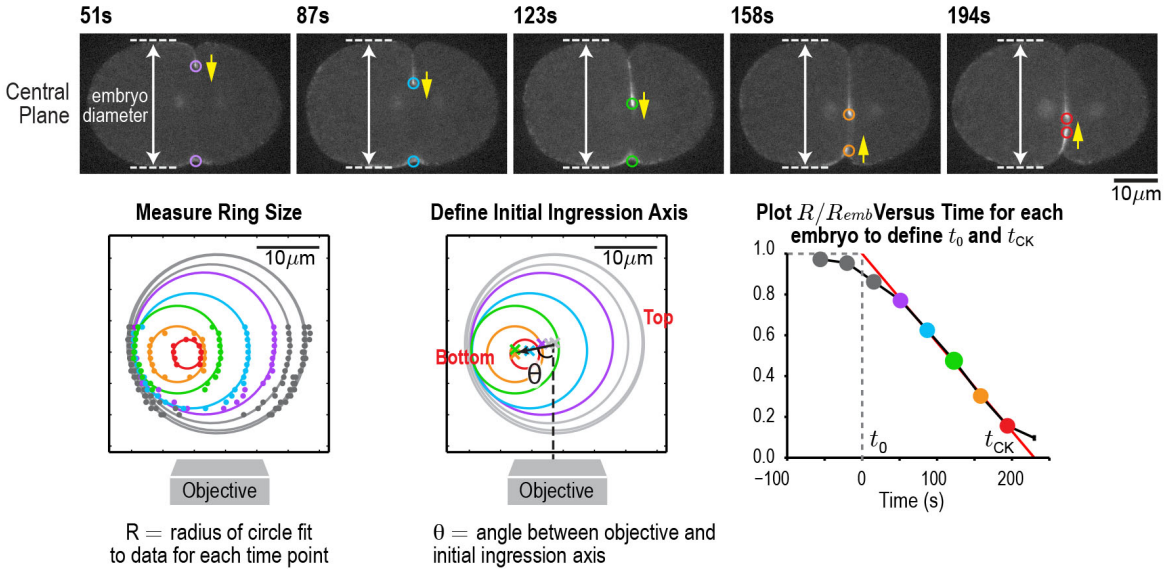

Figure 1 – Figure Supplement 3. An automated method for monitoring contractile ring closure. (*top*) Central plane images of the embryo in Figure 1A. Panels on the lower left and lower right are reproduced from Figure 1A for comparison. An automated algorithm was used to identify the edges of the embryo (dashed lines) and the position of the contractile ring (colored circles) in each z-plane. Yellow arrows mark the direction of furrow ingression and illustrate how the furrow initially ingresses from the top and then changes directions to ingress from the bottom during the second half of cytokinesis. (*lower left*) Points marking contractile ring position in the z-planes were projected onto an end-on view of the division plane. Data for different timepoints in this representative embryo are shown in colors corresponding to the circles in the central plane images. Ring sizes were measured by fitting circles to the data. (*middle*) The initial axis of contractile ring closure was defined by the angle θ between the objective axis and a line fit through the centers of the contractile rings with a normalized size > 0.3. (*right*) = A plot of normalized ring size versus time for this embryo defines t_0 and t_{CK} as the times when a line fit through the points corresponding to ring sizes between 0.3 and 0.8 crossed 1 and 0, respectively. Scale bar is 10μm.

947

Figure 1—figure supplement 4

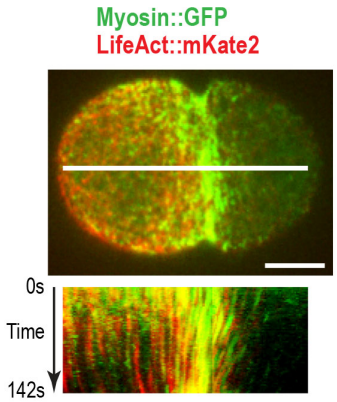

948

949 **Figure 1 – Figure Supplement 4.** Actin and myosin move together with the cortical surface during
950 cytokinesis. The white line in the center of the image (*top*) indicates the region used for the kymograph
951 (*bottom*). Image is representative of 5 imaged embryos. Scale bar is 10µm.

Figure 1—figure supplement 5

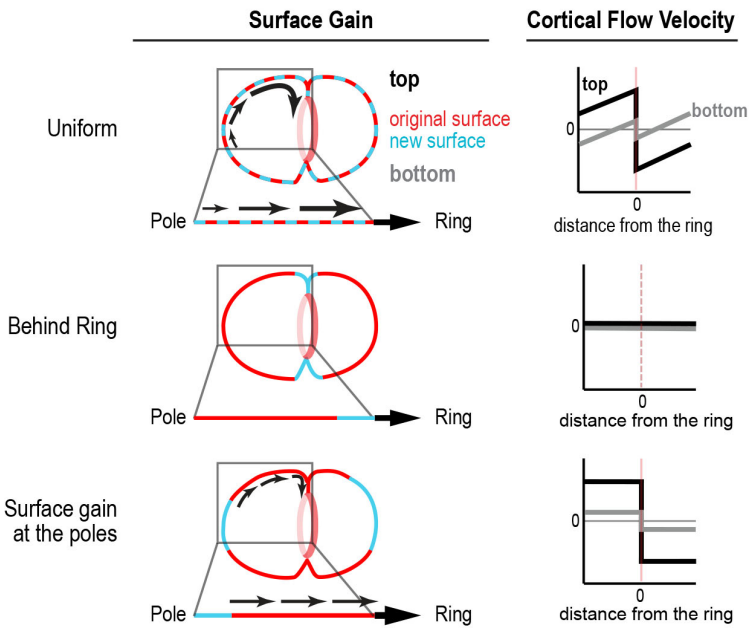

952

953 **Figure 1 – Figure Supplement 5.** Different profiles of cortical surface velocity along the A-P axis are
954 predicted for different spatial patterns of surface gain. (*top*) For surface gain behind the ring, no cortical
955 movement is predicted on the embryo surface. (*middle*) For uniform surface gain, a gradient of velocities
956 will be observed, where the cortex immediately behind the ring moves at the speed of the ingressing
957 furrow, and cortical velocity decreases linearly towards the cell poles. (*bottom*) Reproduced from Figure
958 1B for comparison. If surface is gained only at the poles, cortical velocity will be constant in magnitude
959 within the flow map region with opposite direction on the two sides of the embryo.

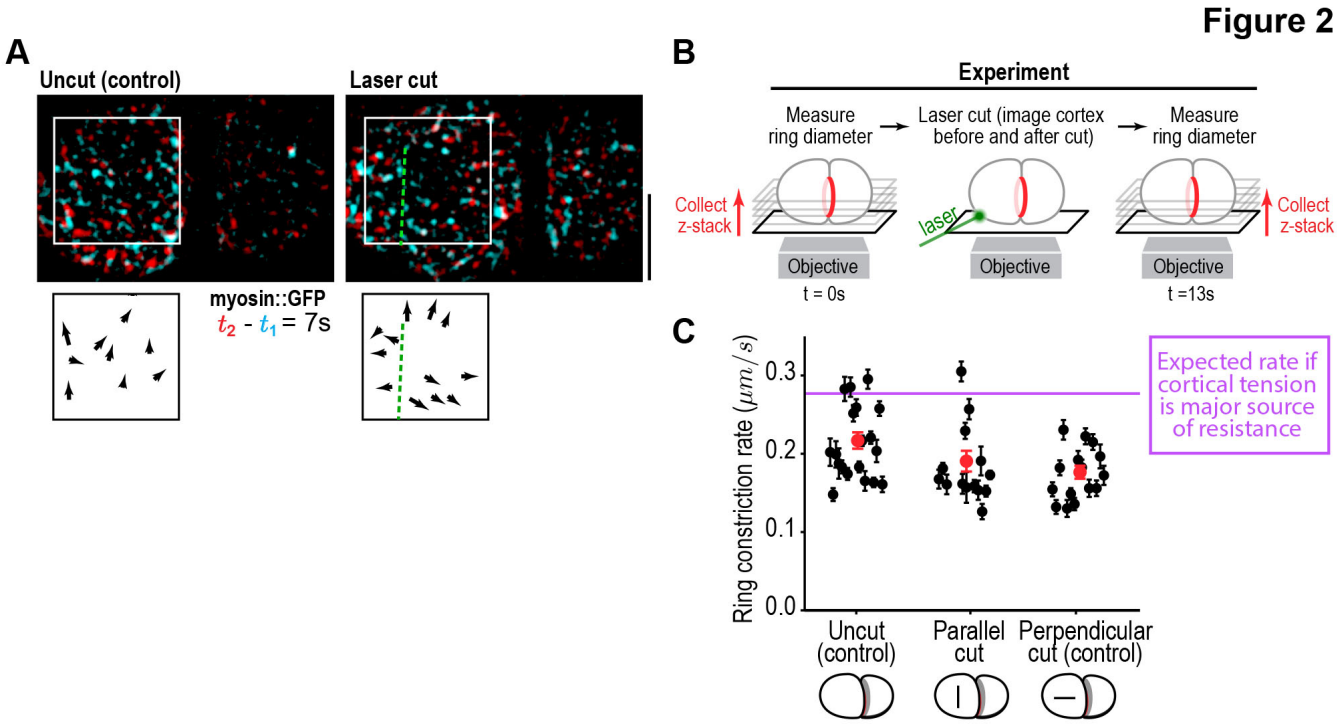

Figure 2. Cortical tension does not limit the rate of ring closure. (**A**) The success of cortical cuts was assessed by comparing surface images of cortical myosin before (*cyan*) and after (*red*) the cut to monitor the movement of myosin foci away from the cut site. Representative images from 1 out of 48 embryos imaged are shown. Scale bar is 10 μm. (**B**) Schematic of laser ablation experiment to determine if cortical resistance limits the rate of contractile ring closure. Contractile ring sizes were measured from z-stacks acquired before and after a cut was made across the cortex with a laser. (**C**) Graph plots the rates of ring closure derived from before and after ring size measurements for uncut controls (n=19 embryos) and embryos with cuts perpendicular (n=15 embryos) or parallel (n=14 embryos) to the ring. Black symbols are single embryo measurements with measurement errors. Red symbols are the means; error bars are the SEM. The purple line marks expected closure rate if cortical tension is a major source of resistance.

Figure 2—figure supplement 1

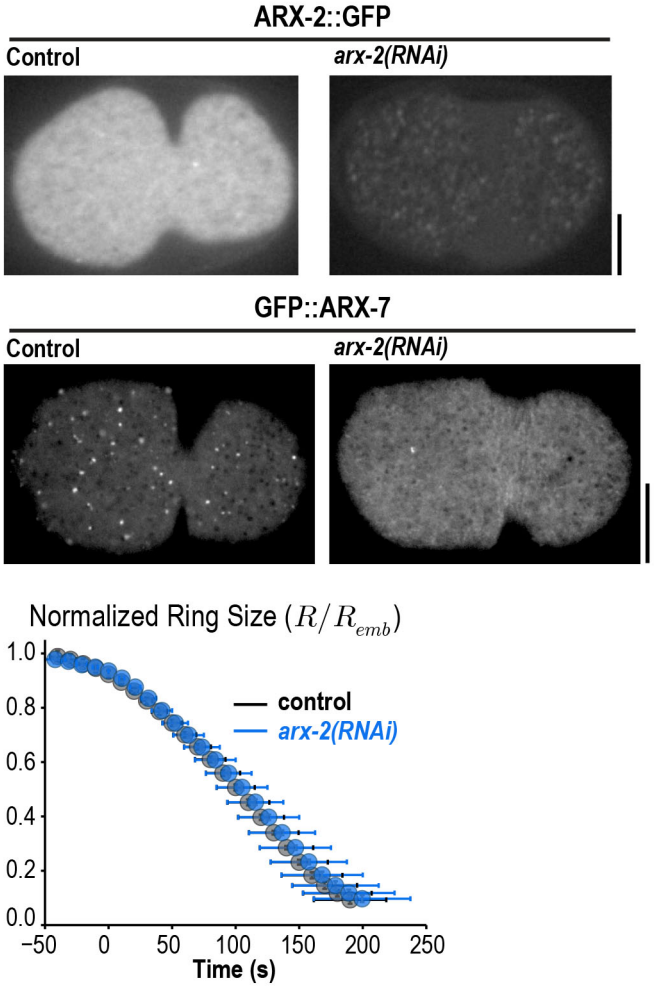

975

976 **Figure 2 – Figure Supplement 1. Arp2/3 depletion does not alter ring constriction kinetics.** Images
977 of cortical ARX-2::GFP and GFP::ARX-7 in control and *arx-2(RNAi)* embryos confirm loss of cortical
978 Arp2/3 complex (images are representative of 10 imaged embryos for each condition in the GFP::ARX-7
979 strain and 15 for control and 13 for *arx-2(RNAi)* in the ARX-2::GFP strain). Scale bars are 10µm. Graph
980 plots average contractile ring size versus time for control (grey) and *arx-2(RNAi)* (blue) embryos
981 expressing myosin::GFP (n= 93 embryos for control and 68 embryos for *arx-2(RNAi)*). Error bars are
982 standard deviation.

983

Figure 2—figure supplement 2

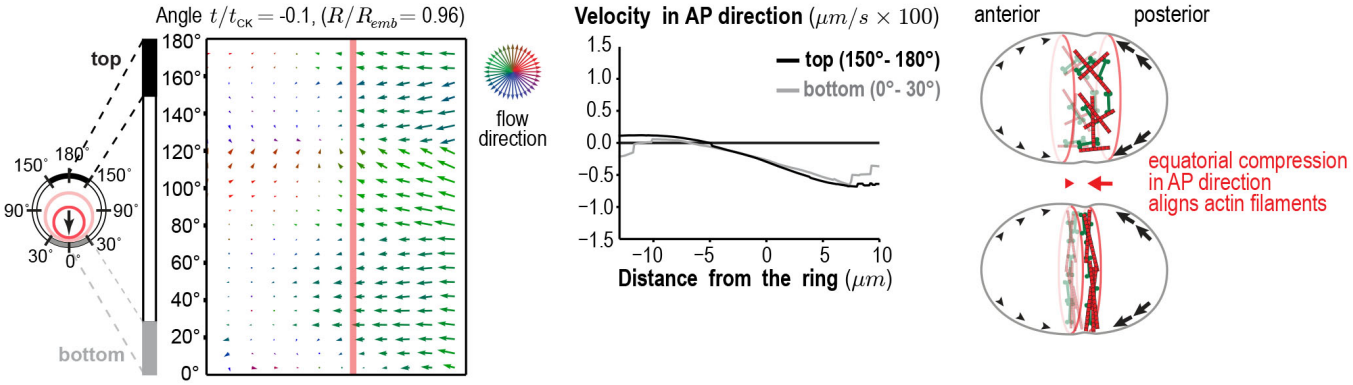

Figure 2 – Figure Supplement 2. An equatorial zone of cortical compression is observed during contractile ring assembly. (*left*) Average flow map at (t/t_{CK}=-0.1) immediately after spindle-based signaling has recruited myosin and other contractile ring components to the equatorial cortex (n= 93 embryos). (*middle*) The surface velocity profile reveals a velocity gradient that spans the cell equator (-5 to +5 μm), indicating a zone of cortical compression. (*right*) Schematic depicting how polar expansion in response to tension generated by the forming ring contributes to equatorial filament alignment during ring assembly.

Figure 3

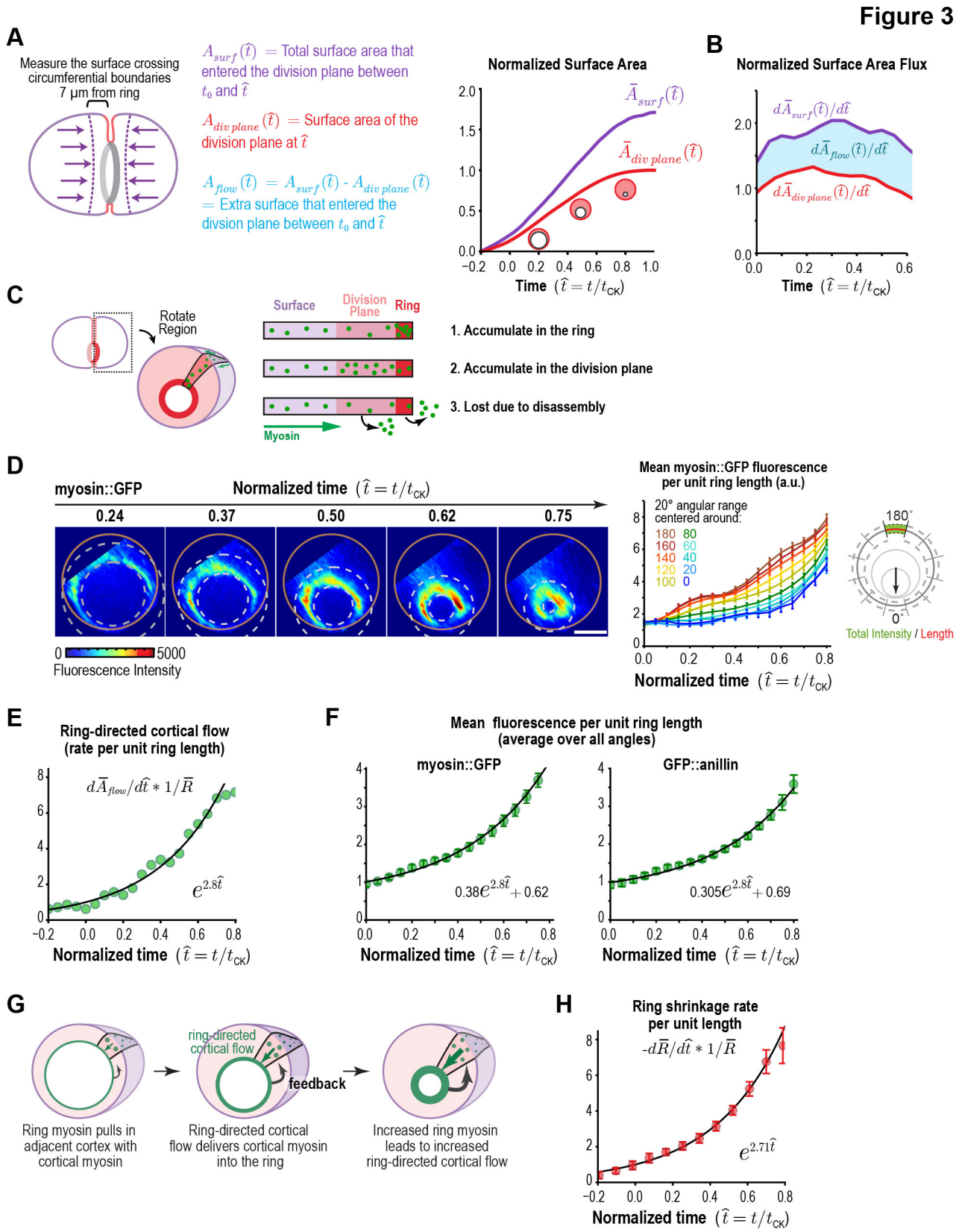

A
Measure the surface crossing circumferential boundaries 7 µm from ring
$A_{surf}(\hat{t})$ = Total surface area that entered the division plane between t_0 and $\hat{t}$
$A_{div\ plane}(\hat{t})$ = Surface area of the division plane at $\hat{t}$
$A_{flow}(\hat{t}) = A_{surf}(\hat{t}) - A_{div\ plane}(\hat{t})$ = Extra surface that entered the divsion plane between t_0 and $\hat{t}$
Normalized Surface Area
$\bar{A}_{surf}(\hat{t})$
$\bar{A}_{div\ plane}(\hat{t})$
Time $(\hat{t} = t/t_{CK})$
B
Normalized Surface Area Flux
$d\bar{A}_{surf}(\hat{t})/d\hat{t}$
$d\bar{A}_{flow}(\hat{t})/d\hat{t}$
$d\bar{A}_{div\ plane}(\hat{t})/d\hat{t}$
Time $(\hat{t} = t/t_{CK})$
C
Rotate Region
Surface
Division Plane
Ring
1. Accumulate in the ring
2. Accumulate in the division plane
3. Lost due to disassembly
Myosin
D
myosin::GFP
Normalized time $(\hat{t} = t/t_{CK})$
0.24
0.37
0.50
0.62
0.75
0
5000
Fluorescence Intensity
Mean myosin::GFP fluorescence per unit ring length (a.u.)
20° angular range centered around:
180 80
160 60
140 40
120 20
100 0
Normalized time $(\hat{t} = t/t_{CK})$
180°
0°
Total Intensity / Length
E
Ring-directed cortical flow (rate per unit ring length)
$d\bar{A}_{flow}/d\hat{t} * 1/\bar{R}$
$e^{2.8\hat{t}}$
Normalized time $(\hat{t} = t/t_{CK})$
F
Mean fluorescence per unit ring length (average over all angles)
myosin::GFP
$0.38e^{2.8\hat{t}} + 0.62$
Normalized time $(\hat{t} = t/t_{CK})$
GFP::anillin
$0.305e^{2.8\hat{t}} + 0.69$
Normalized time $(\hat{t} = t/t_{CK})$
G
Ring myosin pulls in adjacent cortex with cortical myosin
ring-directed cortical flow
feedback
Ring-directed cortical flow delivers cortical myosin into the ring
Increased ring myosin leads to increased ring-directed cortical flow
H
Ring shrinkage rate per unit length
$-d\bar{R}/d\hat{t} * 1/\bar{R}$
$e^{2.71\hat{t}}$
Normalized time $(\hat{t} = t/t_{CK})$

995 **Figure 3. Cortical surface is compressed into the contractile ring during constriction leading to**
996 **an exponential increase in the amount of ring components and in the rates of cortical flow and**
997 **ring constriction.** (**A**) Plot comparing the area of the forming division plane (*red*) with the total cortical
998 surface area that entered the division plane from the start of cytokinesis (*purple*; calculated as indicated
999 in the schematic). (**B**) Plot comparing the rate of cortical flow into the division plane (*purple*) with the rate
000 of division plane growth (*red*). (**C**) Possible fates for extra cortical surface delivered to the division plane.
001 (**D**) (*left*) Images of the division plane reconstructed from 40-plane z-stacks. Gold circles mark the
002 embryo boundary and dashed circles mark the boundaries used for ring intensity measurements. (*right*)
003 Graph plots per unit length myosin::GFP fluorescence for the indicated angular ranges (n=36 embryos).
004 Image series is representative of 36 imaged embryos. (**E,F**) Graphs plot per unit length rate of ring-
005 directed cortical flow (n=93 embryos) and mean per unit length myosin::GFP (n=36 embryos) or
006 GFP::anillin (n=26 embryos) fluorescence (n=36 embryos) in the ring. (**G**) Schematic illustrating the
007 proposed feedback loop that drives the parallel exponential increases in ring myosin and in the rates of
008 cortical flow and constriction. (**H**) Graph plots the per unit length rate of ring closure. Black lines are fitted
009 single exponentials. Error bars are the SEM.
010

Figure 3—figure supplement 1

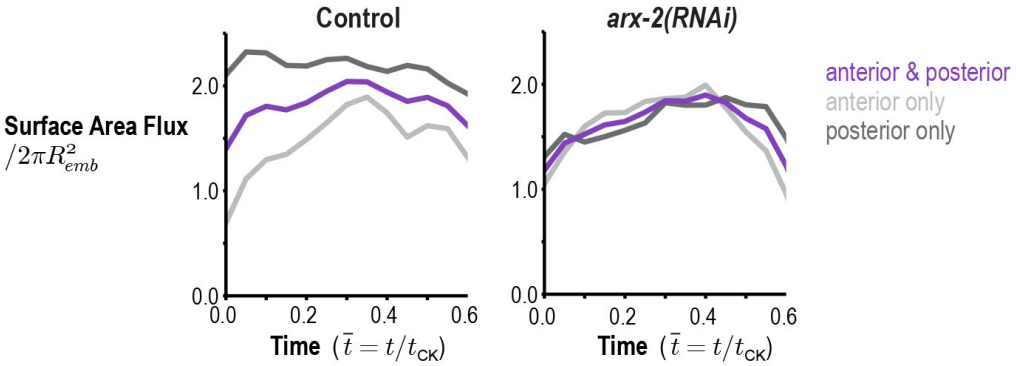

011

012 **Figure 3 – Figure Supplement 1. Arp2/3 inhibition abolishes the asymmetry in the amount of**
013 **cortex entering the division plane from the anterior and posterior sides.** Graphs plot the rate of
014 cortical flux across the anterior (*light grey*) and posterior (*dark grey*) boundaries (see schematic in Figure
015 3A) versus the mean for the two sides (*purple*) for control and *arx-2(RNAi)* embryos. Calculated from the
016 average flow maps for the control (n= 93 embryos) and *arx-2(RNAi)* (n= 68 embryos) conditions.

Figure 3—figure supplement 2

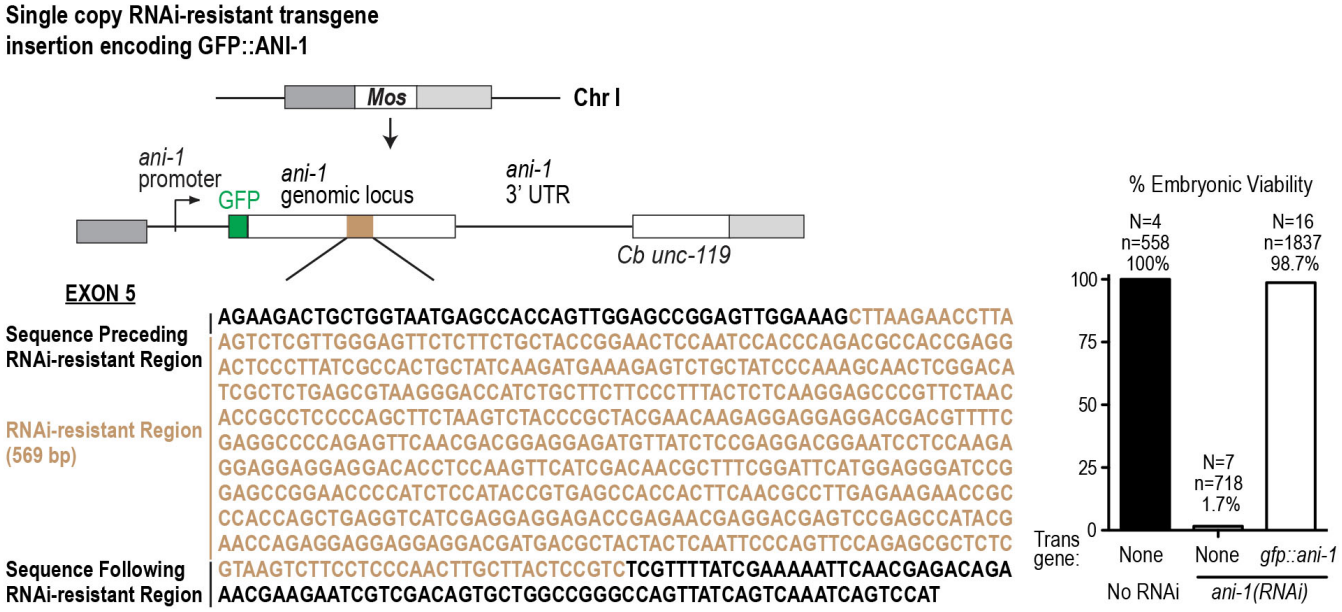

017

018 **Figure 3 – Figure Supplement 2. The GFP::anillin fusion is functional.** (*left*) Schematic of the single-
019 copy *gfp::ani-1* trangene. The transgene was re-encoded while maintaining amino acid sequence in the
020 indicated region to render it resistant to RNAi targeting of the endogenous *ani-1* gene to allow testing of
021 the functionality of the GFP::ANI-1 fusion. (*right*) Graph plotting embryonic lethality demonstrates
022 functionality of the *gfp::ani-1* transgene.

023

Figure 3—figure supplement 3

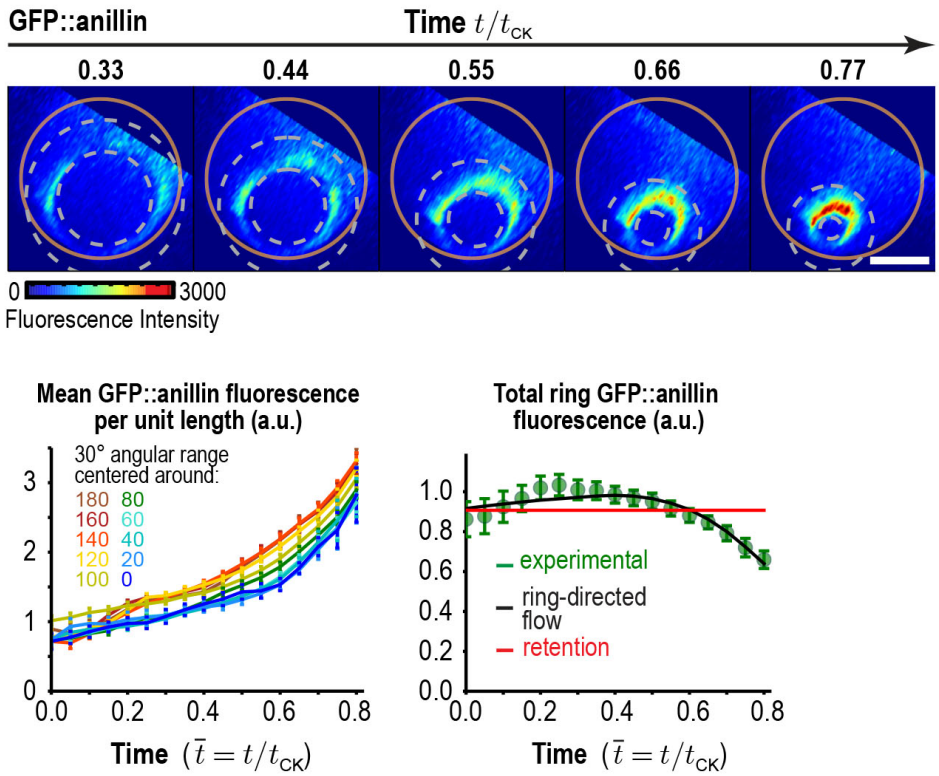

Figure 3 – Figure Supplement 3. GFP::anillin fluorescence in the ring increases exponentially during constriction. (*top*) Images of the division plane in an embryo expressing GFP::anillin. (*bottom, left*) Graph plots GFP::anillin fluorescence per unit length of the ring for the indicated angular ranges. (bottom, *right*) Graph plotting mean total ring fluorescence (average for all angles; *green*) for GFP::anillin (n=26 embryos). The predictions for ring-directed cortical flow (*black*) and the retention (*red*) model are also shown. Error bars are the SEM.

Figure 3—figure supplement 4

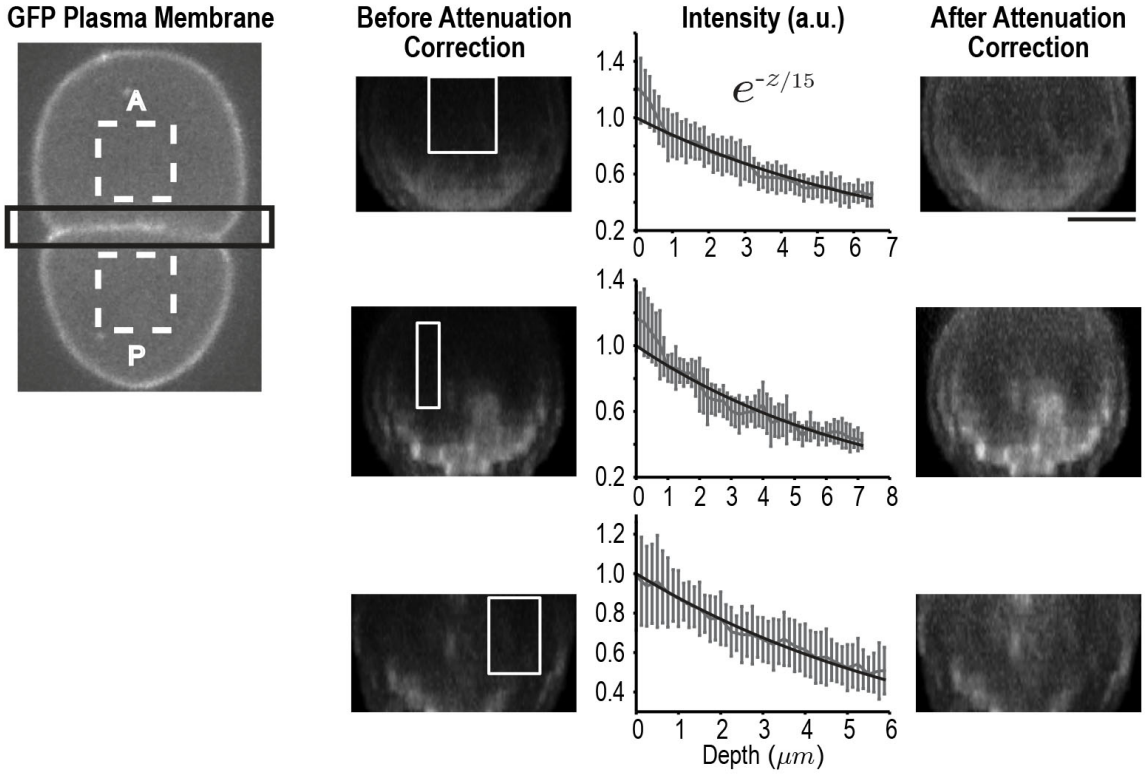

032

033 **Figure 3 – Figure Supplement 4. Correcting for signal attenuation with sample depth.**
034 Fluorescence attenuation with embryo depth was estimated from fluorescence intensity measurements
035 made at the cell-cell boundary of the 2-cell embryos expressing a GFP-tagged plasma membrane
036 marker. Cell-cell boundaries were reconstructed from 40 plane z-stacks. The intensity profile at each
037 slice was calculated by subtracting the average background intensity estimated from dashed rectangles
038 (left) from the cell-cell boundary region (black rectangle) at each slice and calculating the maximum
039 intensity projection along AP axis. The effect of depth on signal was calculated from the reconstructed
040 division planes by plotting the mean signal as a function of depth in 10 rectangular regions (white boxes)
041 where the signal was expected to be uniform; three examples are shown here. All intensity profiles were
042 simultaneously fitted using a single exponential. Error bars are the SD. On the right, the same cell-cell
043 boundaries are shown after correction for depth attenuation. The scale bar is 10 μm.
044

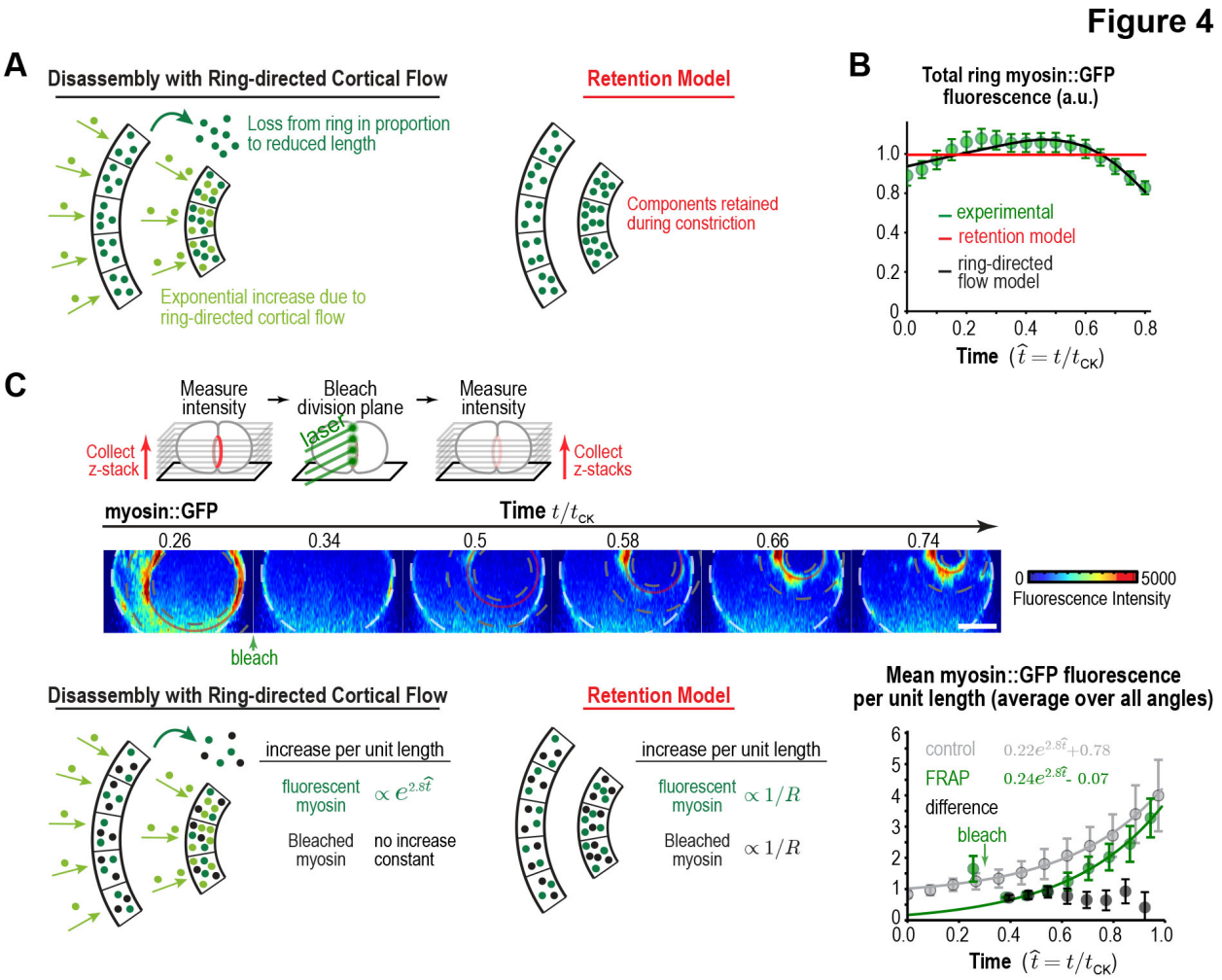

Figure 4. Recovery of myosin::GFP fluorescence after division plane bleaching supports delivery of myosin into the ring by ring-directed cortical flow. (**A**) (*left*) Two models that could explain the increase in the per unit length amount of myosin during constriction. (**B**) Graph plotting mean total ring fluorescence (average over all angles; *green*) for myosin::GFP with the predictions for the ring-directed cortical flow (*black*) and the retention (*red*) models (n= 36 embryos). Error bars are the SEM. (**C**) (*top*) Schematic of the photobleaching experiment to discriminate between the two models. (*middle*) Images of the division plane reconstructed from 30x1μm z-stacks of an embryo expressing myosin::GFP whose division plane was bleached at t/t_{CK} ~0.3. Red circle marks the contractile ring and dashed circles mark the boundaries used for ring intensity measurements. (*bottom left*) Schematics illustrate the expected concentration changes for fluorescent and bleached myosin::GFP. (*bottom right*) Graph plotting the mean per unit length amounts of fluorescent myosin::GFP in the ring for controls (*grey*, n=24 embryos) and after bleaching (*green*, n=8 embryos). The amount of bleached myosin::GFP in the ring (*black*), calculated as the difference between the control and FRAP curves is also shown. Continuous lines are exponential fits to the data. Error bars for controls and FRAP are SD and error bars for the difference are SEM. Scale bar is 10 µm. Image series in (**C**) is representative of 8 imaged embryos.

Figure 4—figure supplement 1

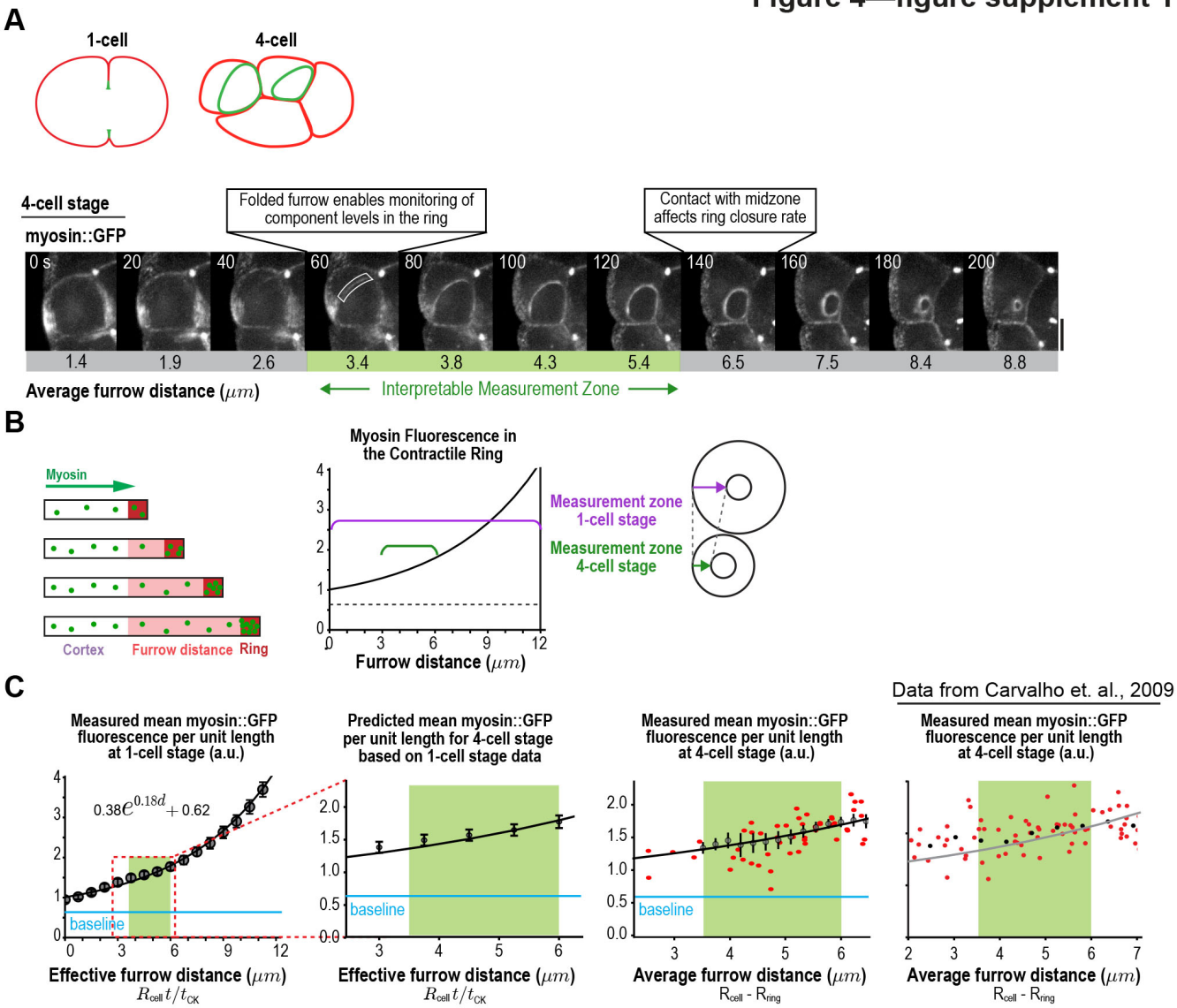

Figure 4 – Figure Supplement 1. Ring component levels in 4-cell stage embryos are consistent with accumulation due to ring-directed cortical flow. (**A**) At the 4-cell stage, cells often divide perpendicular to the imaging plane, providing an "end-on" view of the constricting ring relative to the imaging plane. However, a disadvantage of this division is that ~2/3 of the ring runs along sides of the cell in contact with neighboring cells and cannot be used for measurements. To be able to monitor component dynamics in the entire ring over a larger range of ingression distances, we therefore developed the quantitative tools described in this manuscript to monitor ring constriction at the 1-cell stage. *(top)* Schematic illustrating the relative geometries of cytokinesis in 1- and 4-cell stage *C. elegans* embryos. *(bottom)* images of the division plane in a representative dividing cell at the 4-cell stage reconstructed from 16x1μm z-stacks of an embryo expressing myosin::GFP (n=16 embryos imaged). (**B**) Our 1-cell stage analysis indicates that myosin levels in the ring increase exponentially as a function of furrow distance. The schematics show myosin::GFP fluorescence in the ring as a function of furrow

075 ingression distance at the 1-cell stage, and the predicted change as the furrow ingresses through the
076 interpretable measurement zone at the 4-cell stage if ring myosin accumulates via the same mechanism.
077 Detecting an exponential increase at the 4-cell stage is significantly more difficult than at the 1-cell stage
078 because the cells are smaller and the distance that the furrow ingresses between its formation and when
079 it contacts the spindle midzone, which slows furrowing (Carvalho et al., 2009), is about one quarter of
080 what it is at the 1-cell stage (*Measurement zones*). (**C**) In comparing the 1- and 4-cell stage data, we
081 took advantage of the fact that the initial per unit length constriction rates are the same at the two stages
082 (Carvalho et al., 2009). This makes it possible to predict the pattern of myosin accumulation that we
083 would expect at the 4-cell stage if ring myosin accumulates via the same mechanism that it does at the
084 1-cell stage, and compare it with measured values from the 4-cell stage. (*left panel*) One complication is
085 that, while our 1-cell stage data show that myosin levels increase exponentially as a function of furrow
086 distance, they also suggest there is a baseline of fluorescence (*cyan*) whose precise nature we do not
087 understand—we postulate this baseline could correspond to myosin associated with the plasma
088 membrane but not the cortex. This baseline signal is not part of the exponentially increasing population
089 but influences the measured fold increase in total ring fluorescence. Curve fitting of the 1-cell stage data
090 indicates that the exponentially increasing population increases ~9 fold as the furrow ingresses 12 μm;
091 however, because of the baseline, the measured increase relative to initial ring fluorescence is only ~5-
092 fold. (*middle and right panels*) At the 4-cell stage we can only measure ring component levels for furrow
093 ingression distances between ~3 and 6 μm. The 1-cell data predicts that the exponentially increasing
094 population, which is approximately equal to the baseline at 3 μm, would increase 1.7 fold by 6 μm,
095 resulting in a 1.37-fold increase in total per unit length fluorescence. Fitting both new 4-cell data acquired
096 with the *in situ* tagged myosin::GFP strain that we employed for the 1-cell analysis (*third panel*; n=14
097 embryos) and re-plotting our old data acquired using a myosin::GFP transgene (obtained from (Carvalho
098 et al., 2009); *right panel*) revealed excellent agreement with the predicted curve (*grey line*). Error bars
099 are the SEM. We conclude that data from 4-cell stage embryos are consistent with an exponential
100 increase in ring components during ingression due to ring-directed cortical flow, but technical challenges
101 make clear evidence for an exponential increase significantly more challenging to obtain during this
102 stage relative to 1-cell stage embryos.
103

Figure 4—figure supplement 2

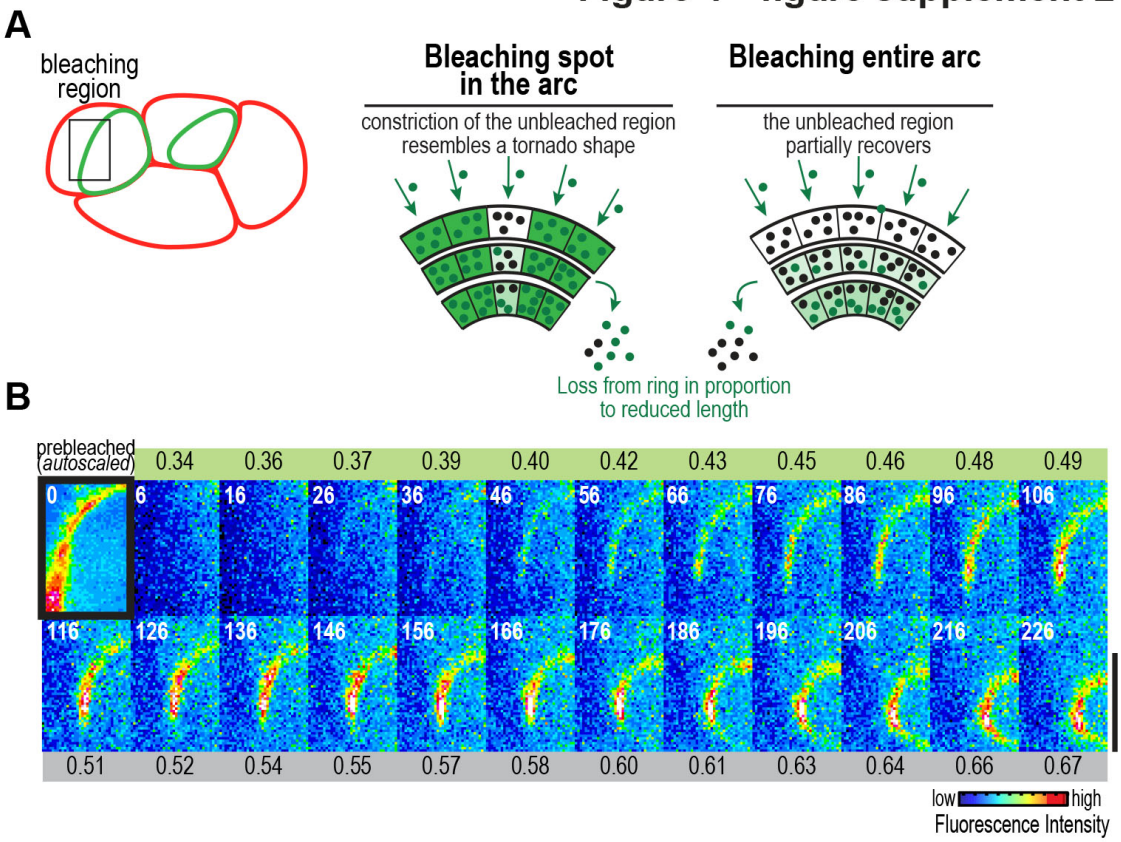

Figure 4 – Figure Supplement 2. Recovery of myosin::GFP fluorescence after division plane bleaching at the 4-cell stage supports delivery of myosin into the ring by ring-directed cortical flow. (**A**) We previously reported that following bleaching of a spot in the arc at the 4-cell stage, the bleached region progressively shrinks, generating a tornado shape in kymographs of a region drawn along the arc, and that the tornado thinning rate was slightly faster than predicted by shrinkage due to ring disassembly alone, which we could not explain (Carvalho et al., 2009). The disassembly with ring-directed cortical flow model that we propose here predicts that after photobleaching a spot in the arc, the unbleached fluorescence in the flanking regions will dominate the fluorescence of the bleached region and ring disassembly will cause the bleached region to progressively shrink, leading to a tornado shape in the kymograph. At the same time, cortical myosin, which turns over faster than myosin in the ring, will recover and ring-directed cortical flow will begin to deliver myosin to the ring again. The increase in ring fluorescence due to cortical delivery would accelerate the rate of tornado thinning consistent with our prior observations. (**B**) As a better test of whether ring-directed cortical flow delivers components to the ring at the 4-cell stage, we monitored recovery after photobleaching the entire contractile arc similar to the experiment that we performed at the 1-cell stage (**Figure 4C**). Images show a representative bleached embryo (n=10). The observed recovery pattern was very similar to what we observed at the 1-cell stage, supporting delivery by ring-directed cortical flow. Scale bar is 10 μm.

Figure 5

A

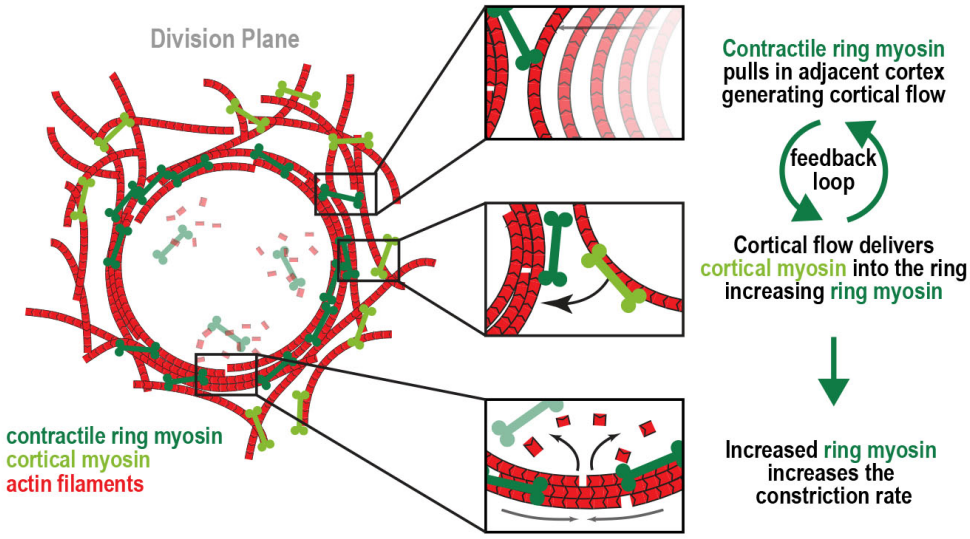

B

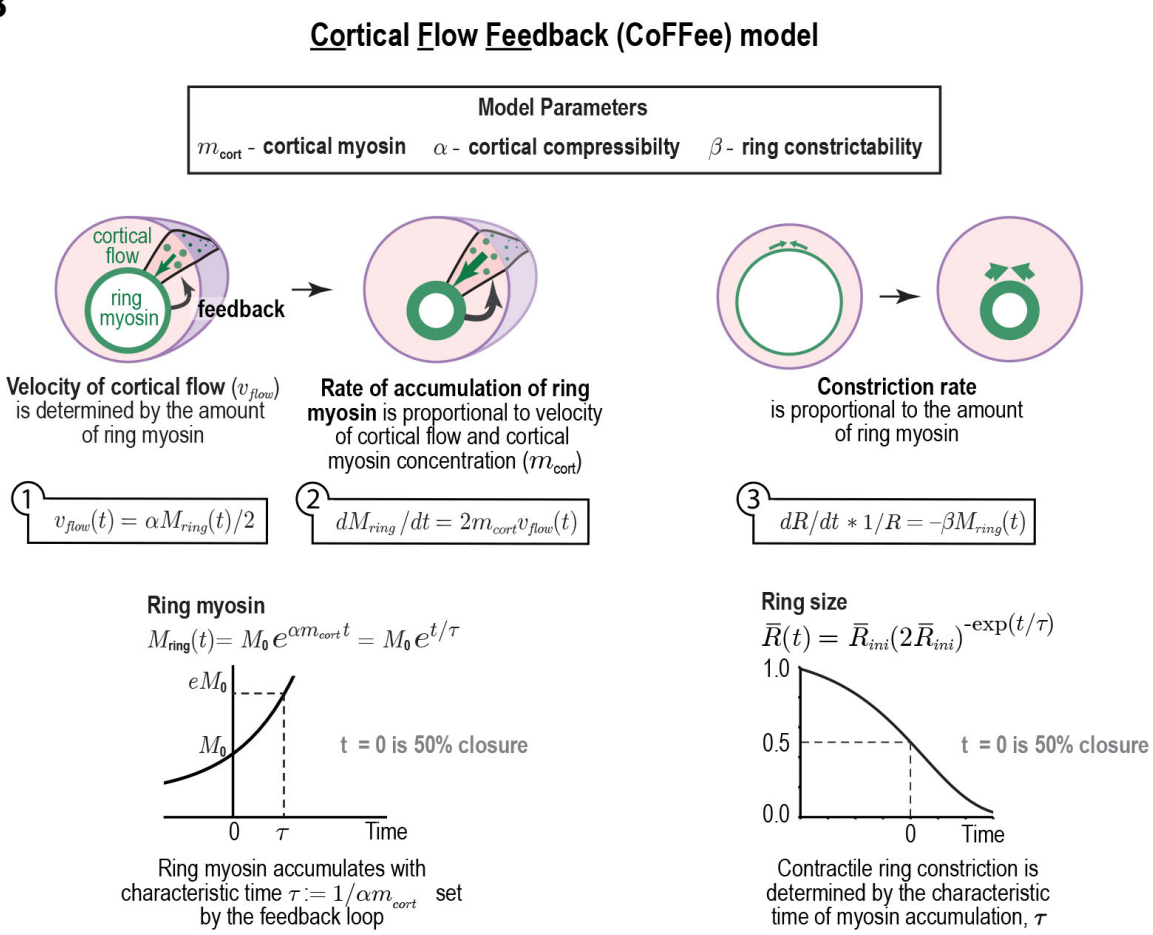

122

Figure 5. Cortical Flow Feedback (CoFFee) model of cytokinesis. (**A**) Schematic model incorporating the conclusions arising from our experimental analysis and proposed underlying molecular mechanism. (**B**) Formulation of the proposed mechanisms as an analytical mathematical model consisting of three equations and three model parameters that reflect properties of the cortex and ring. (*left*) Equations (1) and (2) describe the feedback loop between the amount of ring myosin and the velocity of cortical flow that leads to the exponential increases in the amount of ring myosin and the velocity of cortical flow. (*right*) Equation (3) describes the coupling of ring constriction to the amount of ring myosin.

Figure 6

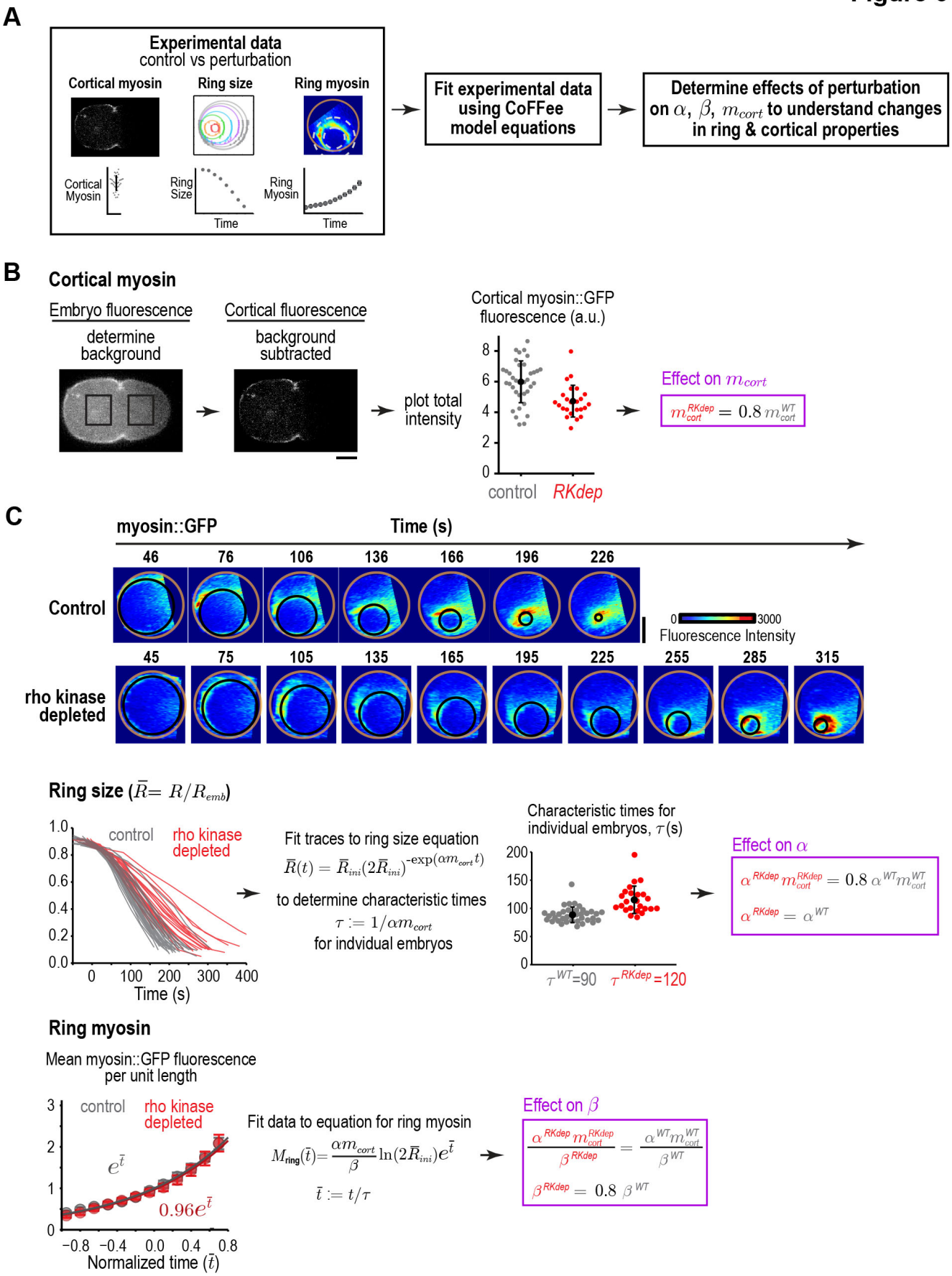
A
Experimental data
control vs perturbation
Cortical myosin
Ring size
Ring myosin
Cortical Myosin
Ring Size
Ring Myosin
Time
Time
Fit experimental data using CoFFee model equations
Determine effects of perturbation on α, β, m_{cort} to understand changes in ring & cortical properties
B
Cortical myosin
Embryo fluorescence
Cortical fluorescence
determine background
background subtracted
plot total intensity
Cortical myosin::GFP fluorescence (a.u.)
control
RKdep
Effect on m_{cort}
$m_{cort}^{RKdep} = 0.8\, m_{cort}^{WT}$
C
myosin::GFP
Time (s)
Control
rho kinase depleted
Fluorescence Intensity
Ring size ($\bar{R} = R/R_{emb}$)
control
rho kinase depleted
Time (s)
Fit traces to ring size equation
$\bar{R}(t) = \bar{R}_{ini}(2\bar{R}_{ini})^{-\exp(\alpha m_{cort} t)}$
to determine characteristic times
$\tau := 1/\alpha m_{cort}$
for indvidual embryos
Characteristic times for individual embryos, τ(s)
τ^{WT}=90
τ^{RKdep}=120
Effect on α
$\alpha^{RKdep} m_{cort}^{RKdep} = 0.8\, \alpha^{WT} m_{cort}^{WT}$
$\alpha^{RKdep} = \alpha^{WT}$
Ring myosin
Mean myosin::GFP fluorescence per unit length
control
rho kinase depleted
$e^{\bar{t}}$
$0.96e^{\bar{t}}$
Normalized time ($\bar{t}$)
Fit data to equation for ring myosin
$M_{ring}(\bar{t}) = \frac{\alpha m_{cort}}{\beta} \ln(2\bar{R}_{ini}) e^{\bar{t}}$
$\bar{t} := t/\tau$
Effect on β
$\frac{\alpha^{RKdep} m_{cort}^{RKdep}}{\beta^{RKdep}} = \frac{\alpha^{WT} m_{cort}^{WT}}{\beta^{WT}}$
$\beta^{RKdep} = 0.8\, \beta^{WT}$

131

Figure 6. Fitting experimental data using the CoFFee model equations reveals the effects of rho kinase inhibition on cortical and contractile ring properties. (**A**) Flow chart illustrating how the CoFFee model can be used to fit experimental data to determine the effects of molecular perturbations on ring and cortical properties. (**B**) (*left*) images illustrating the method used to directly measure cortical myosin::GFP fluorescence. (*right*) Graph plotting cortical myosin::GFP fluorescence for control (*grey*, n=36) and rho kinase depleted (*red*, n=24) embryos. The mean and SD for each condition are shown in black. (**C**) (*top*) Images of the division plane in control and rho kinase depleted embryos expressing myosin::GFP. Gold circles mark the embryo boundaries and black circles mark the contractile ring. Image series shown are representative of the imaged embryos. Scale bar is 10 μm. (*middle, left*) Graphs of ring size traces for individual control (*grey,* n=36) and rho kinase depleted (*red*; n=24) embryos. (*middle, center*). Characteristic times, τ, for individual control (*grey*) and rho kinase depleted (*red*) embryos are plotted along with the mean and SD for each condition (*black*). (*bottom*) Graph plots mean myosin::GFP fluorescence per unit length (averaged over all angles with baseline subtraction) for control (*grey*) and rho kinase depleted (*red*) embryos. Error bars are SEM.

Figure 6—figure supplement 1

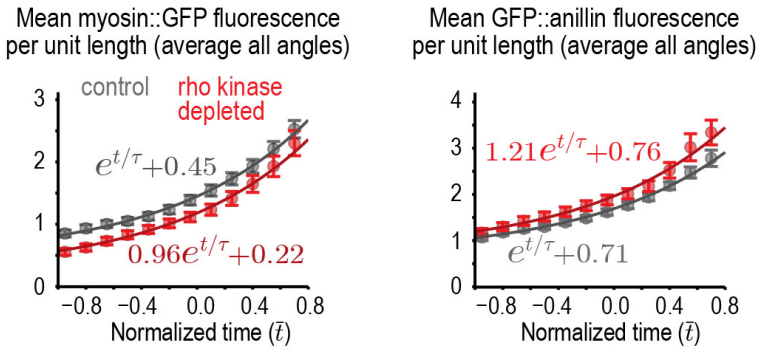

Figure 6 – Figure Supplement 1. Plots of mean myosin::GFP and GFP::anillin fluorescence in the ring versus time. Graphs plotting mean fluorescence per unit length (averaged over all angles) for GFP::anillin and myosin::GFP without baseline subtraction. Error bars are the SEM.

Figure 7

A

Effects of rho kinase depletion (from myosin::GFP data)

mechanical property	model parameter	value relative to wild type
cortical compressibilty	α	WT
cortical myosin	m_{cort}	0.8 WT
ring constrictability	β	0.8 WT

B

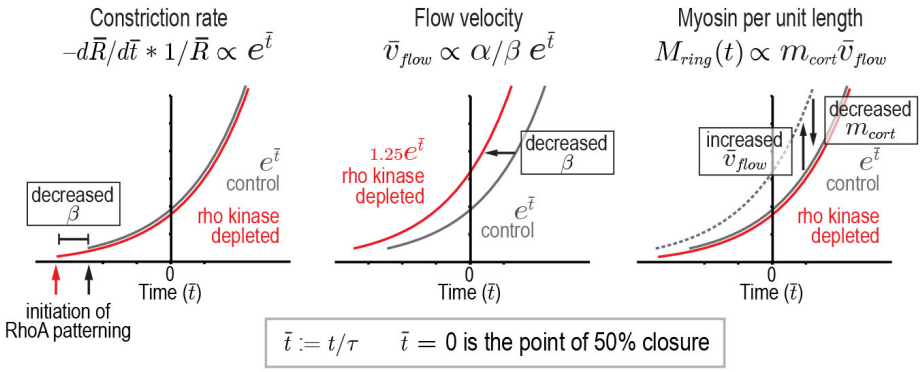

C

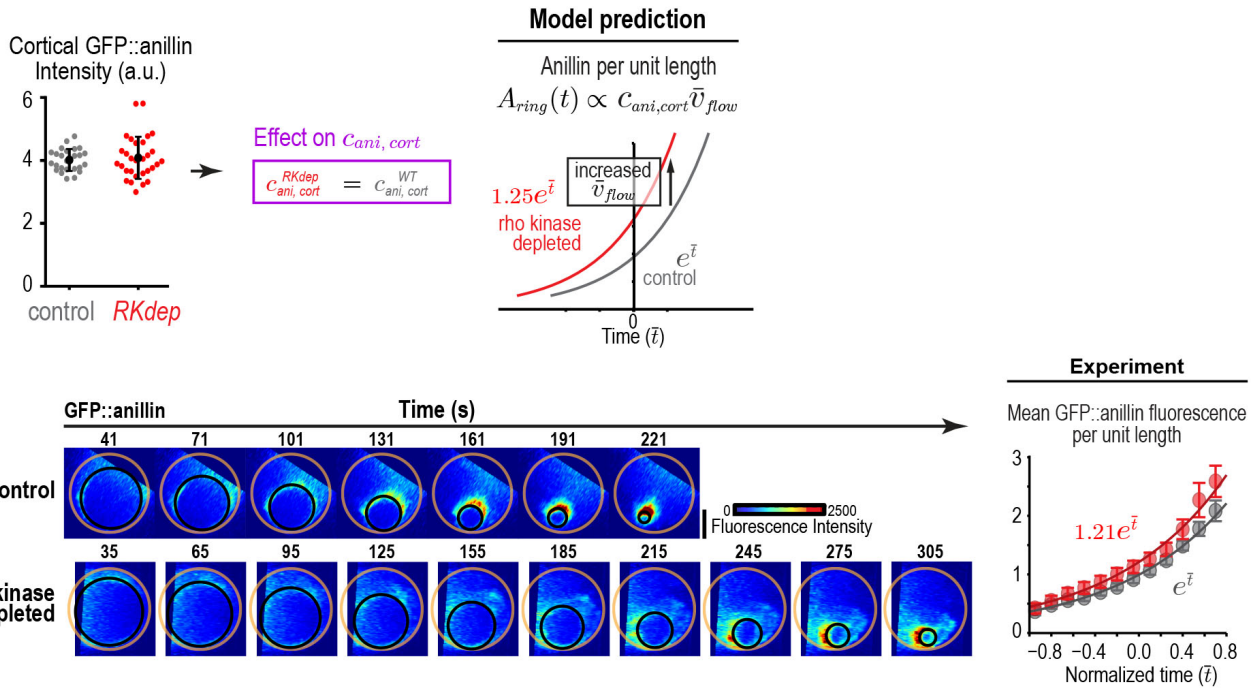

Figure 7. Reducing myosin activation by inhibition of rho kinase reduces the ability of the ring to be constricted by ring myosin. (**A**) (*top*) Table summarizing the effects of rho kinase depletion on model parameters. (**B**) Schematics summarizing the effects of rho kinase inhibition in the reference frame where time is normalized by dividing by τ and $\bar{t} = 0$ is 50% closure. In this time reference, comparing component levels and flow velocity at the same $\bar{t}$ corresponds to comparing them for the same ring size. (**C**) (*top, left*) Graph plotting cortical GFP::anillin fluorescence in control (n=25) and rho kinase depleted (n=30) embryos. The mean and SD are shown in black. (*top, right*) Since the concentration of cortical anillin is not changed, the increased cortical flow in rho kinase depleted embryos is expected to lead to a 1.25-fold increase in the per unit length amount of anillin for rings of all sizes. (*bottom, left*) Images of the division plane in representative control and rho kinase depleted embryos expressing GFP::anillin. Gold circles mark the embryo boundaries and black circles mark the contractile ring. (*bottom, right*) Data for mean GFP::anillin fluorescence per unit length (averaged over all angles with baseline subtraction) for control (*grey*) and rho kinase depleted (*red*) embryos reveals that ring anillin levels are increased 1.21-fold. Error bars are the SEM

Figure 7—figure supplement 1

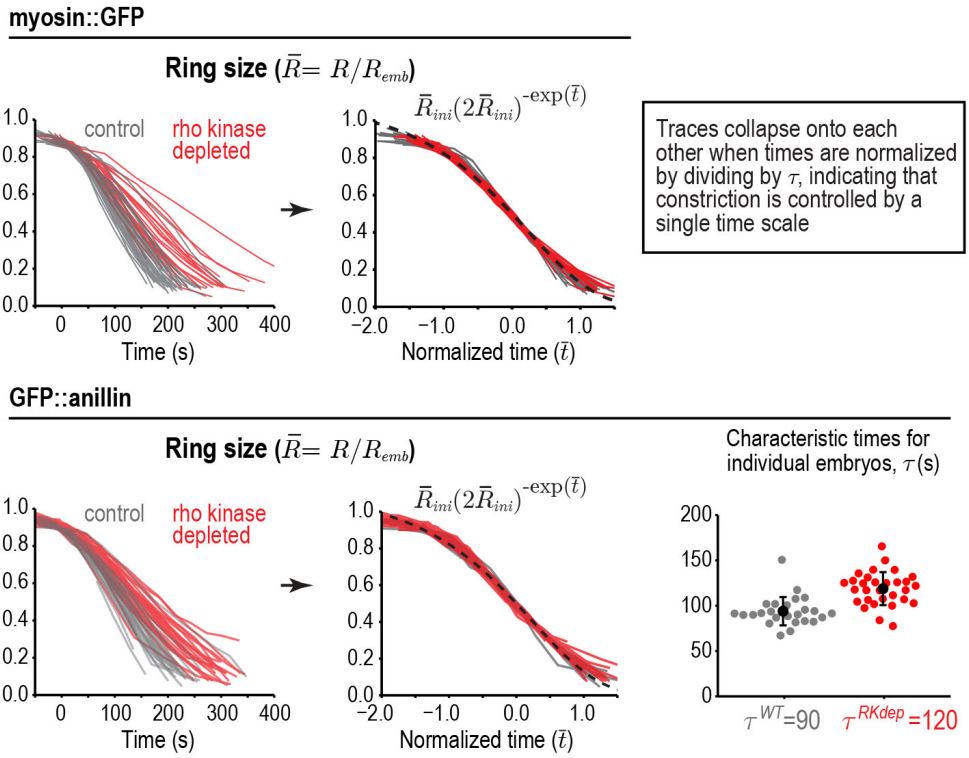

Figure 7 – Figure Supplement 1. Ring constriction is determined by a single time scale. Graphs of ring size traces for individual control (*grey,* n=36 myosin::GFP or 26 GFP::anillin) and rho kinase depleted (*red*; n=24 myosin::GFP or 30 GFP::anillin) embryos. Graph for myosin::GFP expressing embryos is reproduced from Figure 6C for comparison. Traces of ring size for all embryos collapse to the analytical curve (black dashed) when time is normalized by τ and $\bar{t} = 0$ is the point of 50% closure as expected if constriction is controlled by a single time scale. (*bottom, right*) Traces from GFP::anillin

expressing embryos were fit to the ring size equation to determine characteristic times, τ, for individual control (*grey*) and rho kinase depleted (*red*) embryos which are plotted along with the mean and SD for each condition (*black*). Rho kinase depletion increases τ 1.3-fold in GFP::anillin expressing embryos like it does in myosin::GFP expressing embryos.

Figure 7—figure supplement 2

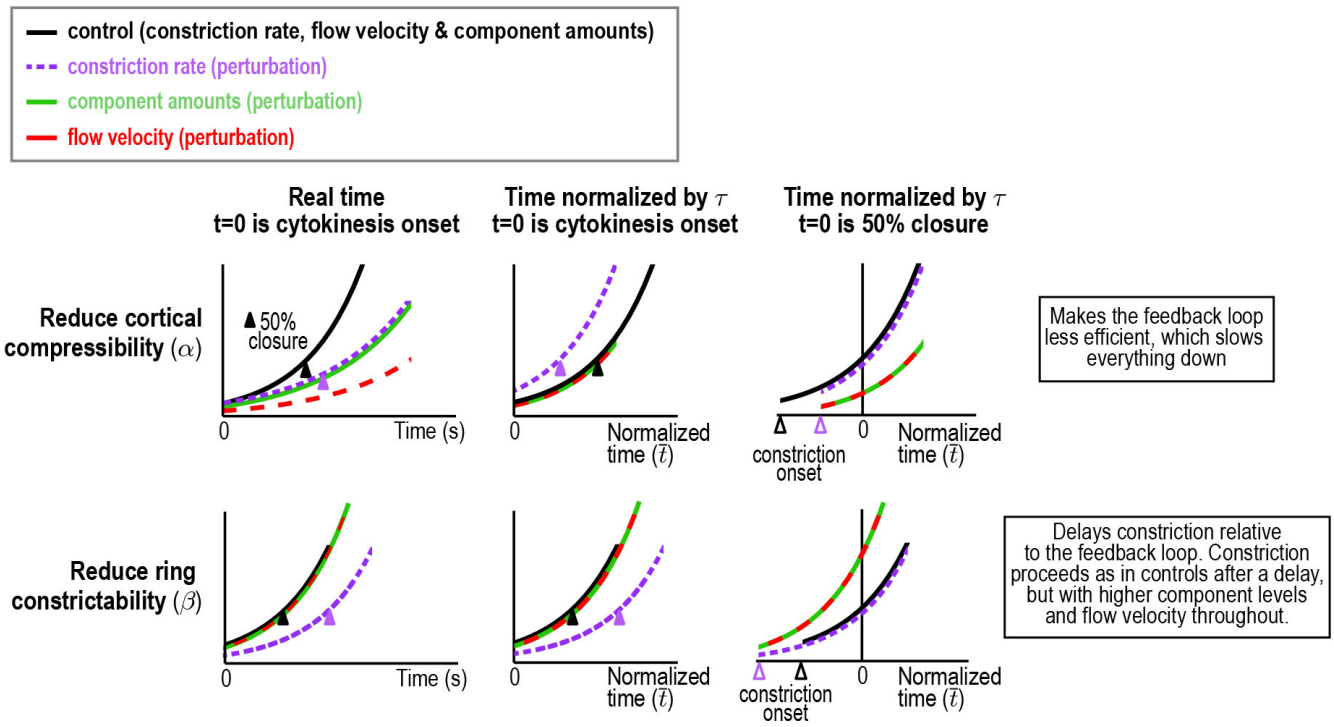

Figure 7 – Figure Supplement 2. Predicted effects of altering properties of the cortex or ring. Schematics illustrate the effects predicted by the CoFFee model of reducing the ability of ring myosin to compress the cortex (*top*) or constrict the ring (*bottom*) on the dynamics of per unit length component amounts (*green*), constriction rate (*purple dashed*) and cortical flow velocity (*red dashed*). The effect on each curve relative to control (*black*) is shown in three time references: real time with t=0 set to constriction onset (*left*), time normalized by τ with t=0 set to constriction onset (*center*), and time normalized by τ with t=0 set to 50% closure (*right*). (*top*) Perturbations that decrease cortical compressibility (α) would increase τ. (*top, right*) In real time, constriction rate and ring component amounts would increase with slower exponential kinetics ($\propto e^{t/\tau}$) from the same starting point as in controls, whereas flow velocity would increase with slower kinetics from a lower starting point ($\propto \alpha e^{t/\tau}$). (*top, center*) Normalizing time by τ, causes rates to be per τ; this increases the flow velocity and constriction rate curves by a factor of $1/\alpha$, bringing the flow velocity back to the control and making the constriction rate start at a higher value than in controls. (*top, right*) Setting t=0 to the 50% closure point superimposes the constriction rate curve with the control, causing the curves for ring component

amounts and flow velocity to fall below the controls. Since comparing properties for the same $\bar{t}$ in this reference is equivalent to comparing properties for a given ring size, reducing α would lead to a reduction in component amounts for all ring sizes. (*bottom*) Reducing ring constrictability (β) does not affect τ. (*bottom, left*) In real time, flow velocity and ring component amounts increase with the same exponential kinetics as controls from the same staring point. The constriction rate also increases with the same exponential kinetics as in controls, but from a lower starting point due to the reduced β. Due to the exponential nature of the curves, the lower starting point effectively introduces a temporal offset, delaying constriction relative to the curves for ring component amounts and flow velocity. (*bottom, center*) Since reducing β does not affect τ, normalizing time by τ does not affect the relationship between the curves. (*bottom, right*) Setting t=0 to the 50% closure point superimposes the constriction rate curve with the control and reveals that reducing β would lead to an increase in component amounts and flow velocity for all ring sizes.

206 **SUPPLEMENTARY VIDEO LEGENDS**

207

208 **Video 1. Cortical flow imaged in a control embryo expressing myosin::GFP.**
209 Playback is 6x realtime. The video is constructed from maximum intensity projection of 3 x 0.75 μm plane
210 z-stacks acquired at 2 s intervals. The red line marks the position of the division plane. The arrows
211 represent the surface movement between consecutive frames at the base of the arrow. The length of the
212 arrow is 5 times the magnitude of movement. The direction is also color coded according to the color
213 wheel as shown in Figure 1b.

214

215 **Video 2. Average cortical flow map calculated from time lapse imaging of the cell surface in 93**
216 **control embryos expressing myosin::GFP.** (*top, left*) Schematic illustrates location of the cylindrical
217 surface covered by the map. (*top, right*) Dynamic schematic illustrates ring size and position for each
218 value of t/t_{CK}. (*bottom, left*) The movement of each blue dot corresponds to surface movement at its
219 location. The y-axis is the angular position relative to the initial ingression axis. The x-axis is the distance
220 from the division plane along the anterior-posterior axis. (*bottom, right*) Dynamic graph plots the
221 magnitude of the component of surface velocity aligned along the anterior-posterior axis for the top (150-
222 180°; black) and bottom (0-30°; grey) regions of the cortex.

223

224 **Video 3. Average cortical flow map calculated from time lapse imaging of the cell surface in 68**
225 ***arx-2(RNAi)* embryos expressing Myosin::GFP.** (*top, left*) Schematic illustrates the location of the
226 cylindrical surface covered by the map. (*top, right*) Dynamic schematic illustrates ring size and position
227 for each value of t/t_{ck}. (*bottom, left*) The movement of each blue dot corresponds to surface movement at
228 its location. The y-axis is the angular position relative to the initial ingression axis. The x-axis is the
229 distance from the division plane along the anterior-posterior axis. (*bottom, right*) Dynamic graph plots the
230 magnitude of the component of surface velocity aligned along the anterior-posterior axis for the top (150-
231 180°; black) and bottom (0-30°; grey) regions of the cortex.